Chapter 1

The NOvA experiment

The NuMI Off-axis ν_e Appearance (NOvA) [1] is a long-baseline neutrino oscillation experiment based at the Fermi National Accelerator Laboratory (Fermilab) [2]. NOvA receives an off-axis ν_μ and $\overline{\nu}_\mu$ beam from Fermilab's Neutrinos from the Main Injector (NuMI) neutrino source (Sec. 1.1) and measures the ν_e or $\overline{\nu}_e$ appearance and the ν_μ or $\overline{\nu}_\mu$ disappearance between its two highly active and finely segmented detectors (Sec. 1.4) [3].

The capability to measure both the ν_e and the $\overline{\nu}_e$ appearance, coupled with a significant matter effect induced by its long baseline, allows NOvA to address some of the most important questions in neutrino physics to date, such as the neutrino mass ordering, the octant of θ_{23}, and the possible Charge conjugation - Parity (CP) symmetry violation in the neutrino sector [3–7]. NOvA data also enables measurements of θ_{13}, θ_{23} and $|\Delta m^2_{32}|$ [3], measurements of neutrino differential cross sections in the Near Detector (ND) [8–11], constraints on the possible sterile neutrino models [12, 13], monitoring for supernova neutrino activity [14, 15], searches for magnetic monopoles [16], or constraints on the neutrino electromagnetic properties (this thesis). Using two functionally identical detectors mitigates the dominant systematic uncertainties of neutrino oscillation measurements, described in Sec. 1.8.

NOvA started taking data in February 2014 and is expected to run through 2026 [17], or until Fermilab begins redirecting its efforts towards the startup of the upcoming Deep Underground Neutrino Experiment (DUNE) experiment [18].

1.1 The Neutrino Beam

The neutrino beam for NOvA comes from the Fermilab-based NuMI neutrino source [19]. The schematic description of NuMI is shown in Fig. 1.1, starting on the left hand side with $120\,\mathrm{GeV}$ protons from the Main Injector (MI), part of the Fermilab accelerator complex. The proton beam is divided into $10\,\mu s$ long pulses, with $\sim 5 \times 10^{13}$ Protons On Target (POT) per spill every $\sim 1.3\,s$ long cycle time, resulting in a proton beam power of $\sim 800\,kW$ (current record $959\,kW$ [20]), with upgrades currently underway to surpass $1\,MW$ [21].

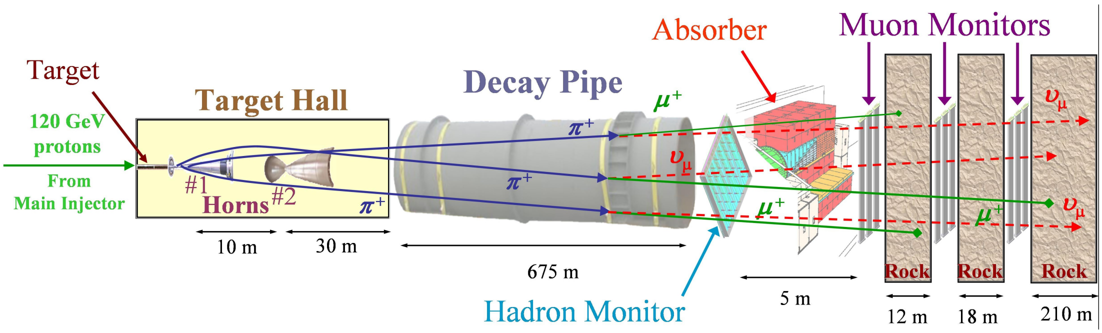

Figure 1.1: The NuMI neutrino beam starts on the left hand side with protons from the MI impinged on a graphite target producing mainly pions and kaons. These are then focused and charge-selected by two focusing horns, after which they decay inside the decay pipe into a high-purity ν_μ or $\overline{\nu}_\mu$ beam. The residual hadrons are stopped and monitored in the hadron absorber and the remaining muons are recorded with muon monitors and absorbed inside the rock. Figure from [19].

The proton beam passes through a collimating baffle before hitting a $\sim 1.2\,m$-long (equal to about two interaction lengths) graphite target [22], producing hadrons, predominantly pions and kaons [19]. These are then focused and selected by two parabolic magnetic 'horns'. The focused hadrons pass through a $675\,m$-long decay pipe filled with helium to create a low density environment for hadrons to propagate and decay in flight into either neutrinos or antineutrinos. High energy hadrons that do not decay in the decay pipe are absorbed within a massive aluminium, steel, and concrete hadron absorber and monitored with a hadron monitor. The leftover muons are ranged out in dolomite rock after the absorber and monitored using three muon monitors. The hadron and muon monitors are ionization chambers, used to monitor the quality, location and relative intensity of the beam.

Using a positive current inside the horns focuses positively charged particles, which then decay into neutrinos, and removes negatively charged particles. Reversing the horn current focuses negatively charged particles, which decay into antineutrinos, and defocuses positively charged particles. The neutrino mode is therefore called Forward Horn Current (FHC) and the antineutrino mode is called Reverse Horn Current (RHC). The composition of the neutrino beam for both these modes at the NOvA ND is shown in Fig. 1.2, displaying the very high purity of the ν_μ or $\overline{\nu}_\mu$ component in the FHC ro RHC beam respectively [19].

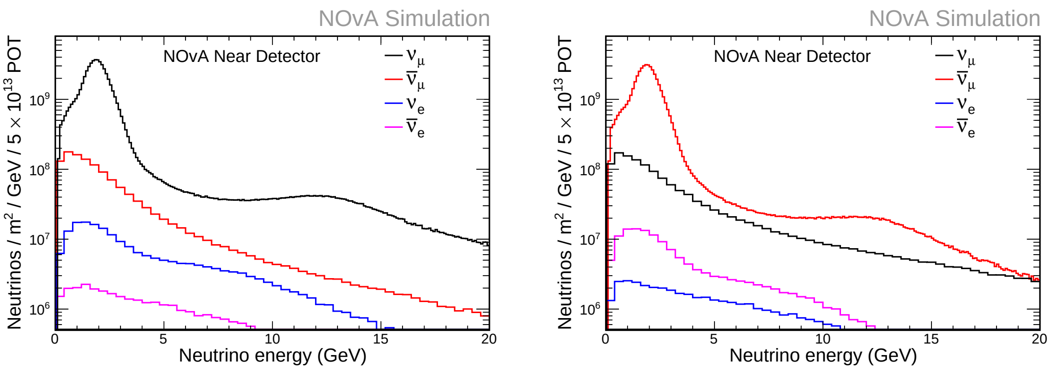

Figure 1.2: The components of the neutrino beam at the NOvA ND per one NuMI spill in the FHC regime shown on the left and the RHC regime on the right. The ν_μ ($\overline{\nu}_\mu$) composition in the FHC (RHC) regime is 93.8% (92.5%), with a wrong sign contribution of 5.3% (6.6%) and only 0.9% (0.9%) contamination by ν_e ($\overline{\nu}_e$), showing the high purity of ν_μ and $\overline{\nu}_\mu$ in the neutrino beam for NOvA. Beam composition values calculated for neutrinos with energies between $1 - 5\,\mathrm{GeV}$. Figures are from internal NOvA repository [23].

The resulting neutrino beam energy distribution is peaked at $\sim 7\,\mathrm{GeV}$ with a wide energy band. However, thanks to the kinematics of the dominant pion decay, by placing the NOvA ND and Far Detector (FD) $14.6\,\mathrm{mrad}$ ($\approx 0.8\,°$) off the main NuMI beam axis, NOvA achieves a narrow band neutrino flux peaked at $1.8\,\mathrm{GeV}$ [7, 24], as can be seen in Fig. 1.3. Using an off-axis neutrino flux increases the neutrino beam around $2\,\mathrm{GeV}$ about 5-fold compared to the on-axis flux and narrow-band peak enhances background rejection for the ν_e appearance analysis [24].

1.2 The NOvA Detectors

The two main NOvA detectors are the ND, located in Fermilab $\sim 1\,\mathrm{km}$ from the NuMI target and $\sim 100\,\mathrm{m}$ under ground, and the FD, located $\sim 810\,\mathrm{km}$ from Fermilab at Ash River in north Minnesota, partially underground with a rock overburden [24]. NOvA also operated a detector prototype called Near Detector on the Surface (NDOS), which was used for early research and development of detector components and analysis [4]. Additionally, NOvA operated a Test Beam detector, described in detail in Sec. ??. The scales of the ND and FD are shown in Fig. 1.4.

All NOvA detectors are highly segmented, highly active, functionally identical

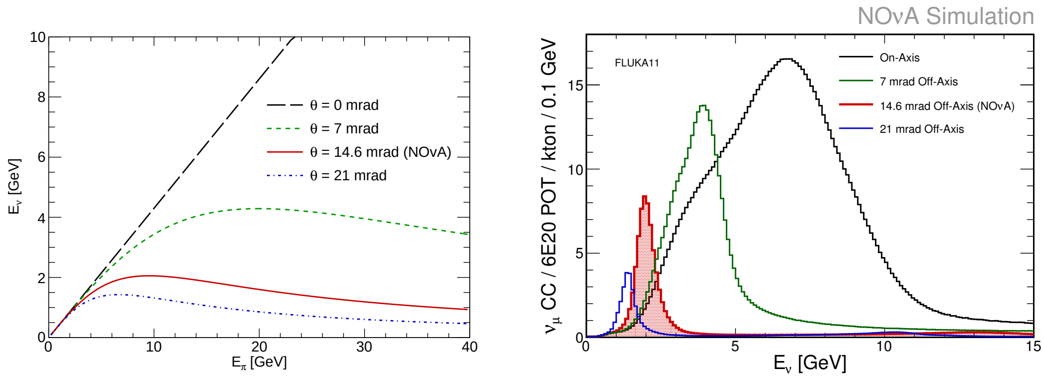

Figure 1.3: (Left) Dependence of the neutrino energy on the parent pion's energy and (right) neutrino energy distribution for an on-axis beam and three different off-axis beam designs. The case for NOvA is shown in red and results in a narrow neutrino energy distribution around 2 GeV, with limited dependence on the parent pion's energy. Figure from [24]

tracking calorimeters made up of Polyvinyl chloride (PVC) cells filled with liquid scintillator. Each cell is a long rectangular cuboid with depth of $5.9\,\mathrm{cm}$ and width of $3.8\,\mathrm{cm}$ (with some variations), with cell length extending to the full width/height of each detector, which is $\sim 4.1\,\mathrm{m}$ for the ND and $\sim 15.6\,\mathrm{m}$ for the FD [24]. An example of a FD cell is shown on the right of Fig. 1.4.

Cells are connected side-by-side into a 16 cell-wide extrusions with $3.3\,\mathrm{mm}$-wide walls between cells and $4.9\,\mathrm{mm}$-wide walls on the outsides of the extrusions. The first and last cell of each extrusion are $\sim 3\,\mathrm{mm}$ narrower than the rest of the cells. Two extrusions are connected side-by-side to form a 32 cell-wide module, with each module having a separate readout (see Sec. 1.3). In the FD, 12 modules are connected side-by-side to form one plane of the detector. In the ND only 3 modules make up a plane. Planes are positioned one after another, alternating between vertical and horizontal orientation, and grouped into diblocks, each containing 64 planes. The FD contains 14 diblocks, totalling 896 planes, whereas the ND contains 3 diblocks totalling 192 planes. The ND also contains a Muon Catcher region, positioned right after the active region, consisting of 22 planes of the normal NOvA detector design, 2 modules high and 3 modules wide, sandwiched with 10 steel plates to help range out muons mainly from the ν_μ charged current interactions [4, 24].

The NOvA coordinate system is centred with $(0,0,0)$ in the centre of the first plane, relative to the beam direction. The x axis runs from left to right when facing the detector, y axis from bottom to top and z axis runs perpendicular to the planes

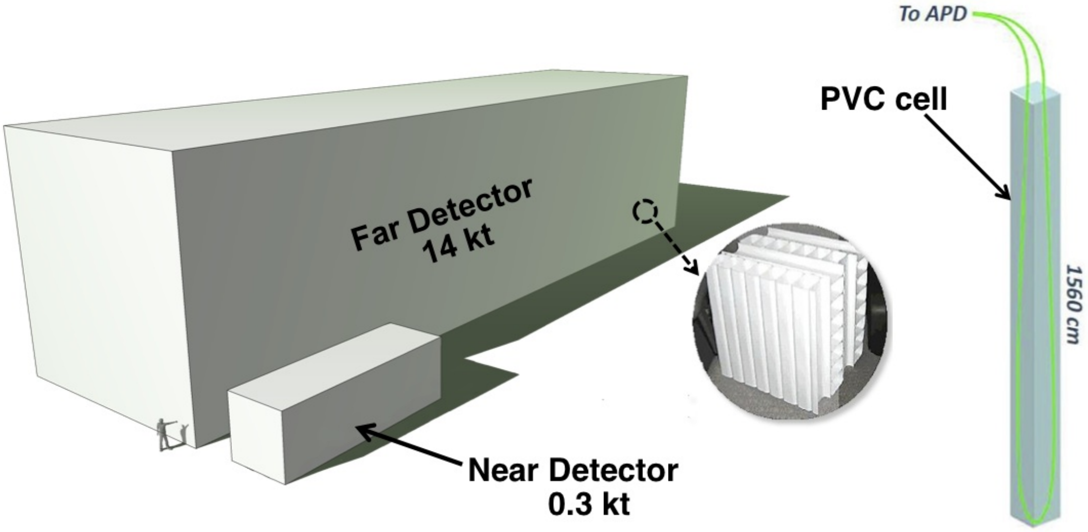

Figure 1.4: Schematic description of the scale and composition of the NOvA ND and FD. The inset shows a photo of the orthogonal planes made out of PVC cells. An example of a FD cell containing liquid scintillator and a looped WLS fibre attached to an APD is shown on the right [25].

along the beam direction.

Each cell is filled with a liquid scintillator consisting of mineral oil with 4.1% pseudocumene as the scintillant [26]. Each cell contains a single wavelength shifting fibre with double the length of the cell, looping at one end and connecting to the readout at the other. The PVC walls of the cells are loaded with highly reflective titanium dioxide, with light typically bouncing off the PVC walls ~ 8 times before being captured by the Wavelength Shifting (WLS) fibre [24].

The final dimensions of the FD are $15.6\,\mathrm{m} \times 15.6\,\mathrm{m} \times 60\,\mathrm{m}$ with a total mass of $14\,\mathrm{kT}$ and for the ND the dimensions are $3.8\,\mathrm{m} \times 3.8\,\mathrm{m} \times 12.8\,\mathrm{m}$ with a mass of about $0.3\,\mathrm{kT}$ [17]. The active volume, consisting only of the liquid scintillator without the PVC structure, makes up about 70% of the total detector volume [24].

The NOvA detectors are specifically designed for electromagnetic shower identification, with a radiation length of $38\,\mathrm{cm}$, which amounts to ~ 7 planes for particles travelling perpendicular to the detector planes [4]. This is particularly useful to distinguish electrons from π^0s.

We can calculate the minimum energy an electron needs to have to cross one cell ($5.9\,\mathrm{cm}$) of the NOvA detector by using the measured scintillator density $0.86\,\mathrm{g/cm^3}$ [27], which gives us the required range of $\sim 5\,\mathrm{g/cm^2}$. Comparing this to measured values for the electron range [28] in the continuous slowing down approximation in a Polyethylene (approximation of the NOvA scintillator [29]), gives us an estimate of the lowest detectable electron energy as $E_e \gtrsim 10\,\mathrm{MeV}$.

1.3 Readout and Data Acquisition

The signal from the WLS fibres is read out by an Avalanche Photodiode (APD), converting the scintillation light into electrical signal, with a high quantum efficiency of $\sim 85\%$ and a gain of 100 [24]. An example APD is shown in Fig. 1.5. Both ends of each fibre correspond to a single readout channel and are connected to one of the 32 pixels on the APD, organized in four rows of 8 pixels, with each APD reading out signal from one module. To maximise the signal to noise ratio, the APDs are cooled to $-15\,^{\circ}\mathrm{C}$ by a thermoelectric cooler, with heat carried away by a water cooling system.

The combination of the APD quantum efficiency and the light yield, determined by the PVC reflectivity and the scintillator and WLS fibre responses, result in a signal requirement of at least 20 Photo Electron (PE) in response to minimum ionizing radiation at the far end of the FD cell.

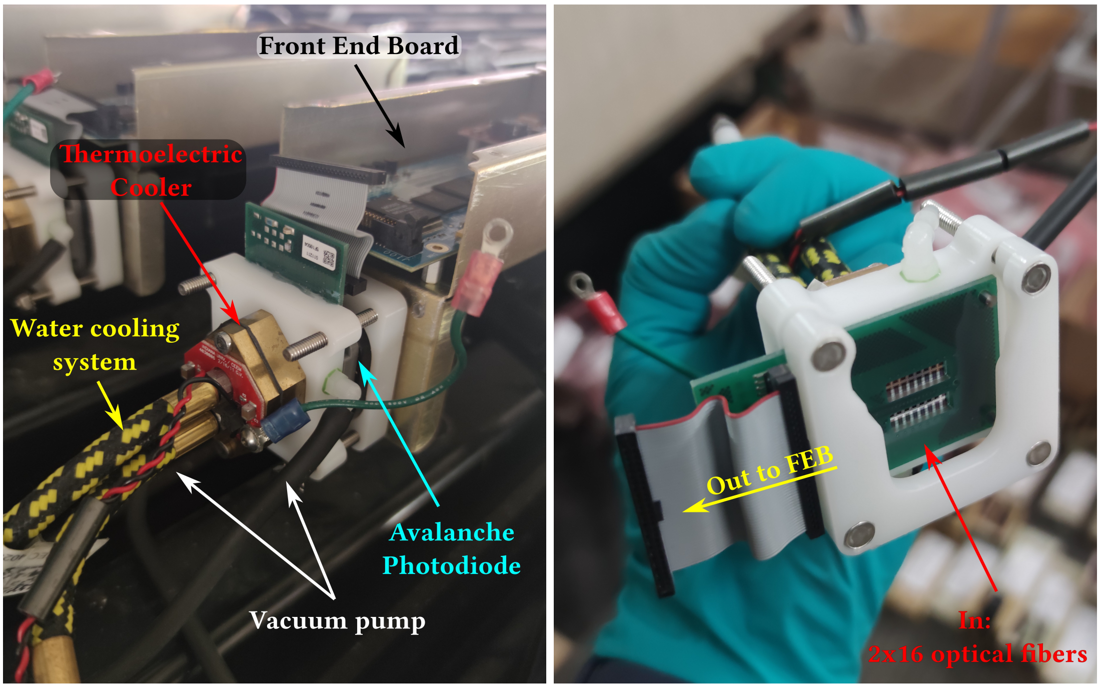

Figure 1.5: The modules with APDs for NOvA mounted on top of the detector on the left picture, and shown from the bottom on the right. The individual components of the module are described. The left picture shows a disconnected ribbon cable and ground cable, which are normally connected to the front end board.

Each APD is connected to a single Front End Board (FEB), shown in Fig. 1.6. The

FEB amplifies and integrates the APD signal, determines its amplitude and arrival time, before passing it to the Data Acquisition (DAQ) system. On the FEB the APD signal is first passed to a custom NOvA Application-Specific Integrated Circuit (ASIC), which is designed to maximize the detector sensitivity to small signals. ASICs amplify, shape and combine the signal, before sending it to an Analog-to-Digital Converter (ADC). The combined noise from the APD and the amplifier is equivalent to about 4 PEs, which, compared to an average PE yield from the far end of the FD cell of 30, results in a good signal and noise separation [24]. The digitized data from an ADC is sent to a Field Programmable Gate Array (FPGA), which extracts the time and amplitude of the ADC signals, while subtracting noise based on a settable threshold. The FPGAs employ multiple correlated sampling methods to reduce noise and improve time resolution of the signal [30].

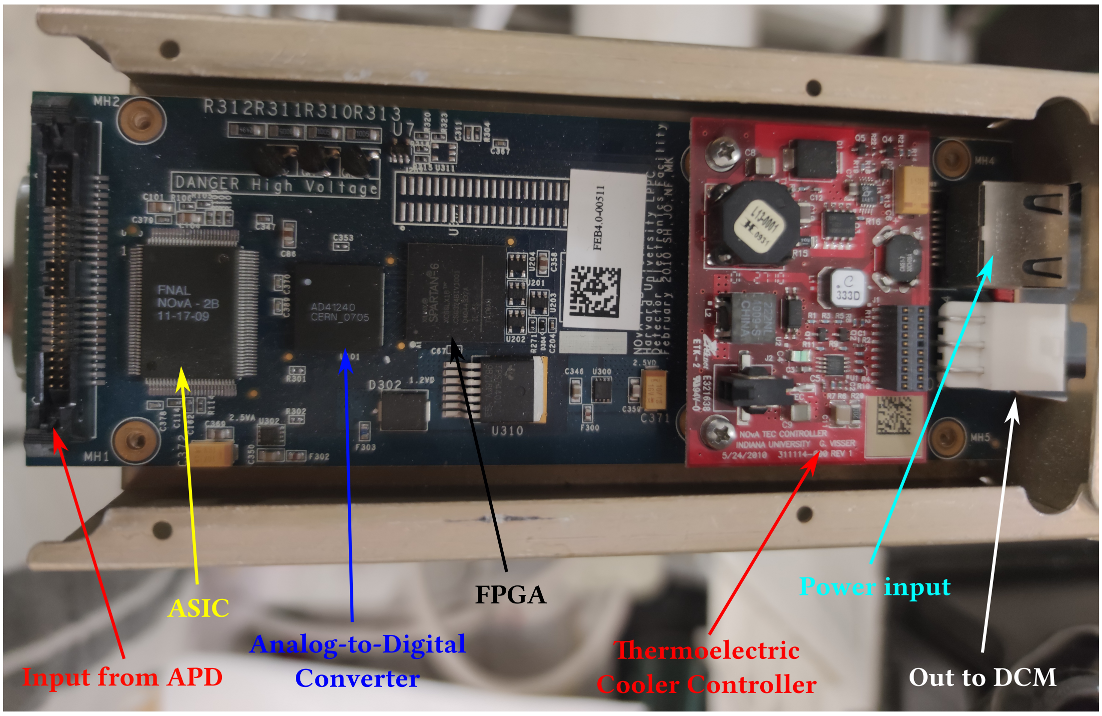

Figure 1.6: An example of a NOvA FEB with individual components labelled.

All of the NOvA front end electronics (APDs and FEBs) are operated in a continuous readout mode, without requiring any external triggers [24]. Due to higher detector activity during beam spills, the ND FEBs work at a higher frequency of 8 MHz, whereas the FD FEBs suffice with 2 MHz sampling frequency [30].

Data from up to 64 FEBs are concentrated in a Data Concentration Module (DCM), which concatenates and packages the data into 5 ms time slices, before sending it to the buffer nodes. DCMs are also connected to the timing system and pass a single unified timing measurement to the FEBs to maintain synchronization across the detector [30].

The buffer nodes cache the data for at least 20 seconds while receiving information from the trigger system. Each trigger uses a time window based either on the time of the NuMI beam spill, on a periodic interval for monitoring and for the readout of cosmic events, or on one of the activity-based data-driven triggers [30]. Data that fall within any of the trigger windows are sent to a data logger system, where they are merged to form events, before being written to files for offline processing and sent to an online monitoring system. Files are organized based on a unique combination of run and subrun numbers, with runs corresponding to data taking periods with constant detector conditions and limited to either 64 subruns or 24 hours. Subruns are delineated either by a 2 GB file size constraint or a 1-hour timeout limit [31].

The detectors are continuously monitored to ensure data stability and quality. Subruns with suboptimal detector conditions or with events failing basic quality criteria are flagged as 'bad' and recorded in a 'bad runs list' [31]. Additionally, individual readout channel are assessed on a per-subrun basis, with those with too high or too low hit rates marked as 'bad' [32]. Both the 'good runs' list and the 'bad channel' maps are used to inform event processing and during simulation to emulate real detector conditions.

1.4 Simulation

To extract neutrino oscillation parameters, or to test a hypothesis, NOvA uses a series of simulations to make predictions according to various physical models [33]. The simulation chain can be divided into four parts: simulation of the neutrino beam, simulation of neutrino interactions within the NOvA detectors, simulation of cosmic particles interacting in the NOvA detector and simulation of the detector and readout response.

To simulate the neutrino beam, NOvA uses a simulation based on the GEANT4 v9.2.p03 [34] Monte Carlo (MC) event generator with a detailed model of the NuMI beamline [35], as described in Sec. 1.1. The simulation starts with the $120\,\mathrm{GeV/c}$

MI protons interacting within the long carbon target and producing hadrons, mainly π, K and secondary protons. This is followed by transport and possible further interaction of hadrons within the focusing system, until finally ending with hadron decays producing the neutrino beam.

To account for the inherently imprecise theoretical models used in GEANT4, NOvA uses the Package to Predict the Flux (PPFX) to incorporate external measurements of yields and cross sections of hadron interactions inside the target and the other NuMI materials into the neutrino beam prediction [36]. The current version of PPFX is limited by the results available during its creation and only corrects the most frequent interactions while assigning conservative systematic uncertainties to the rest (see Sec. 1.8). For the most common π, K and p production, PPFX uses the NA49 measurements [37–39] of $158\,\mathrm{GeV/c}$ protons interacting on a thin (few percent of interaction length) carbon target. To expand the kinematic coverage, PPFX uses a few data points from Barton et al [40] for the π production and K/π ratios from the Main Injector Particle Production (MIPP) [41] experiment for the production of K. These results have to be scaled to the $20 - 120\,\mathrm{GeV/c}$ incident proton moment seen throughout NuMI using the FLUKA [42, 43] MC generator.

There are two new experiments that measure the production and interaction of hadrons on various targets and incident energies, specifically designed to improve the prediction of neutrino beams. The most impactful measurements from the NA61 experiment are of the $120\,\mathrm{GeV/c}$ protons on a thin carbon target [44–46], of the hadron incident interactions [47], and of the $120\,\mathrm{GeV/c}$ protons on a NuMI replica target [48]. The Fermilab-based EMPHATIC experiment [49] is currently analysing a broad range of hadron production and secondary and tertiary interaction measurements for neutrino beam prediction with a significant involvement of NOvA and DUNE collaborators.

The output of the neutrino beam simulation is passed to the simulation of neutrino interactions inside the detectors, which is done with the GENIE v3.0.6 [50] neutrino MC generator. GENIE allows users to choose the particular models for different types of neutrino interactions and particle propagation within the nucleus, as well as possible tunes to external measurements. The four main interaction modes in GENIE are the Quasi-Elastic (QE) Charged Current (CC) scattering, the Resonant baryon production (Res), the Deep Inelastic Scattering (DIS), and the Coherent π (COHπ). The special case of the two particle - two hole (2p2h) interaction via Meson Exchange Current (MEC) and the Final State Interaction (FSI) inside the nucleus are also considered. The initial state of the nucleus is represented by a local Fermi gas in the QE and 2p2h models, while a global relativistic Fermi gas is used for all other processes. All of these are set by the Comprehensive Model Configuration (CMC), which is currently `N1810j0000` for NOvA. Additionally, NOvA adds a costume tune to the NOvA ν_μCC data for a better constraint of the CCMEC interactions. NOvA also uses a set of external π interaction measurements to constrain the FSI model. Table 1.1 shows the list of models and tunes for different interaction modes in NOvA [7].

Table 1.1: Models and tunes used in the NOvA simulation of neutrino interactions.

Interaction	Model	Tune
CCQE	València [51]	External $\nu - \mathrm{D}$ data [52]
CCMEC	València [53, 54]	NOvA ν_μCC data
Res & COHπ	Berger-Sehgal [55, 56]	External $\nu - A$ data
DIS	Bodek-Yang [57, 58]	External $\nu - A$ data
FSI	Semi-classical cascade [59]	External $\pi -^{12}$ C data

Since the FD is on the surface NOvA also uses a simulation of cosmic rays generated with the MC Cosmic-Ray Shower Generator (CRY) [60]. The simulated cosmic muons are also used to calibrate NOvA detectors [36].

Particles that are created from neutrino interactions and cosmic rays are propagated through the NOvA detectors using the GEANT4 v10.4.p02 [34], which outputs the energy deposited in the scintillator. This is then passed to a custom NOvA software of the light model [36], which calculates the amount of scintillation light produced for the deposited energy based on a Poisson distribution. The scintillation light production is parametrized using the Birks-Chou model [61], which corrects for the recombination in organic scintillators at high deposited energies. The scintillator light yield and the inherent production of the Cherenkov light, which can affect the light readout, are tuned to NOvA data [9]. The light collection by the WLS fibres, its transport to the APDs, and the APD response use a parametrized simulation, as the NOvA cells and their readout are generally the same across the detectors [36]. The simulation of the readout electronics is done by another custom NOvA parametrized model, which accounts for random noise in the readout electronics and outputs true events in the same format as the real data.

Due to the high neutrino rate in the ND, there are neutrinos interacting in the surrounding rock creating particles, mainly muons, that make it to the detector and act as background. However, since only a few 'rock muons' make it into the detector, it would be very time consuming to run a simulation which includes the rock around the ND for every neutrino. Instead, NOvA creates a separate simulation that includes the surrounding rock and then overlays these results into the nominal NOvA simulation chain to match the NuMI neutrino rate [36].

1.5 Data Processing and Event Reconstruction

Both data and simulation events for all NOvA detectors are passed through the same event reconstruction and particle identification algorithms. The reconstruction was specifically developed with the ν_e appearance search in mind, focusing on identifying the ν_eCC signal against the ν_μCC and Neutral Current (NC) backgrounds. Each NOvA detector has to deal with different challenges, with multiple neutrinos interacting during one beam spill in the ND, and a large cosmic background in the FD [62].

The output from the DAQ system for each channel is called a *raw hit*. Hits are grouped into 550 μs-long windows and passed to an offline reconstruction chain [62]. Reconstruction starts by grouping hits into *slices* based on their proximity to other hits in both time and space [63]. Slices are designed to ideally contain only a single neutrino interaction event.

For events that produce hadronic and electromagnetic showers, reconstruction first identifies straight lines through major features using a modified Hough transform [64], representing particle directions. These lines are passed to the Elastic Arms algorithm [65] to identify *vertex* candidates from their intersection points. Hits are then clustered into *prongs*, which are collections of hits with a start point, based on the vertex, and a direction, using a k-means algorithm called FuzzyK [66, 67]. Here 'fuzzy' means that each hit can belong to multiple prongs. Prongs are first created separately for each view (also called 2D prongs) and then, if possible, view-matched into 3D prongs (from here on referred to as prongs) [62]. Figure 1.7 shows an example of a simulated electron shower, where the reconstructed vertex is shown as a red cross and the prong as a red shaded area. The prong groups together all the hits that are part of the shower, while removing the background hits, shown in grey.

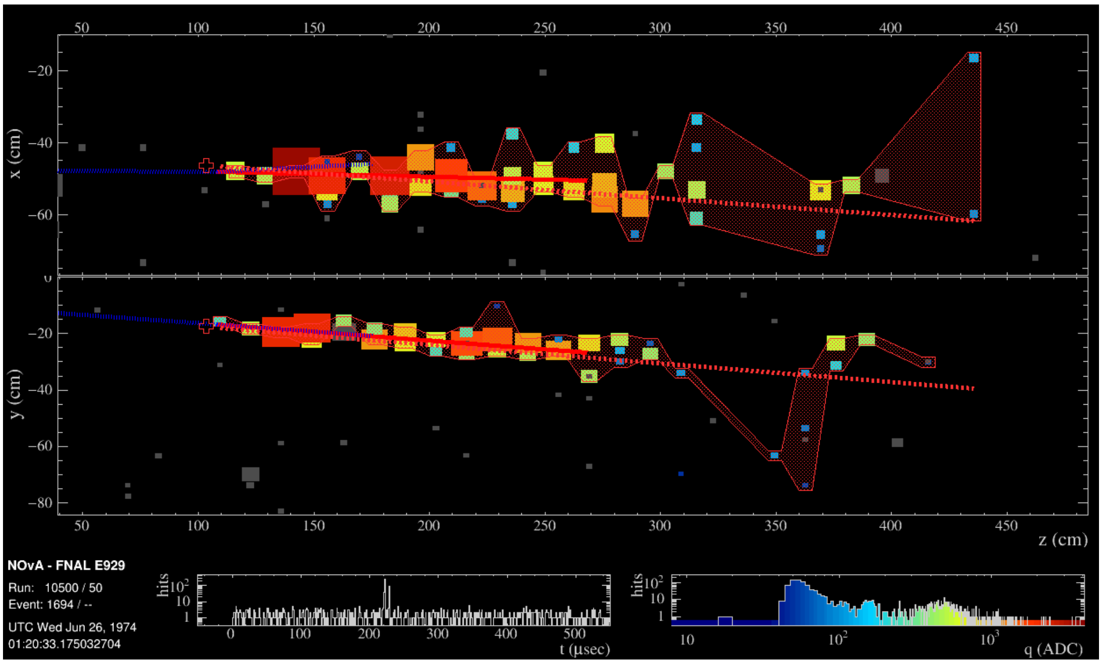

Figure 1.7: Reconstruction of a simulated single electron event in the NOvA ND. The red cross is the reconstructed vertex, the shaded area shows the cluster of hits into a prong and the dotted red line shows the estimated shower direction. The blue dotted line shows the true direct of the scattering neutrino and the solid red line the true momentum of the scattered electron. Figure from internal NOvA database [68].

For particles that are represented by tracks rather than showers (especially muons), the reconstruction takes the slice hits and forms 'Kalman tracks' based on a Kalman filter [69]. In addition to the start point and the direction, which exist also for prongs, tracks also contain information on the vector of trajectory points that make up the track and on the end point - and therefore on the track length. A parallel tracking algorithm takes in the Elastic Arms vertex and the Fuzzy-K prongs and forms Break Point Fitter (BPF) tracks [70, 71], using a model of Coulomb scattering and energy loss. BPF tracks also contain an information on the particle 4-momenta based on various particle assumptions, most notably the muon assumption. For cosmic particles, mostly muons, NOvA uses another track reconstruction algorithm, called 'window cosmic track' [72]. It uses a sliding 5 plane-long window, in which it fits a straight line to the recorded hits. The window starts from the end of the detector and then slides forward and repeats the fitting process until all hits are processed. This way it accounts for possible Coulomb scattering of cosmic muons. The intersection of each cosmic track with the edge of the detector (or extrapolation of the track to the edge of the detector) is reconstructed as the 'cosmic ray vertex'.

To identify individual particles and remove backgrounds, NOvA uses several Machine Learning (ML) algorithms, outputs of which are used in combination with the information from classical reconstruction algorithms for Particle Identification (PID). The most common topologies for particles interacting in NOvA detectors are shown in Fig. 1.8. Muons are easily identifiable as single long tracks which decay into an electron (or positron) if stopping inside of the detector. Both electrons and π^0's produce electromagnetic showers, but thanks to the low-Z composition and high granularity of the detector, there is a gap between the interaction vertex and the electromagnetic shower for the π^0.

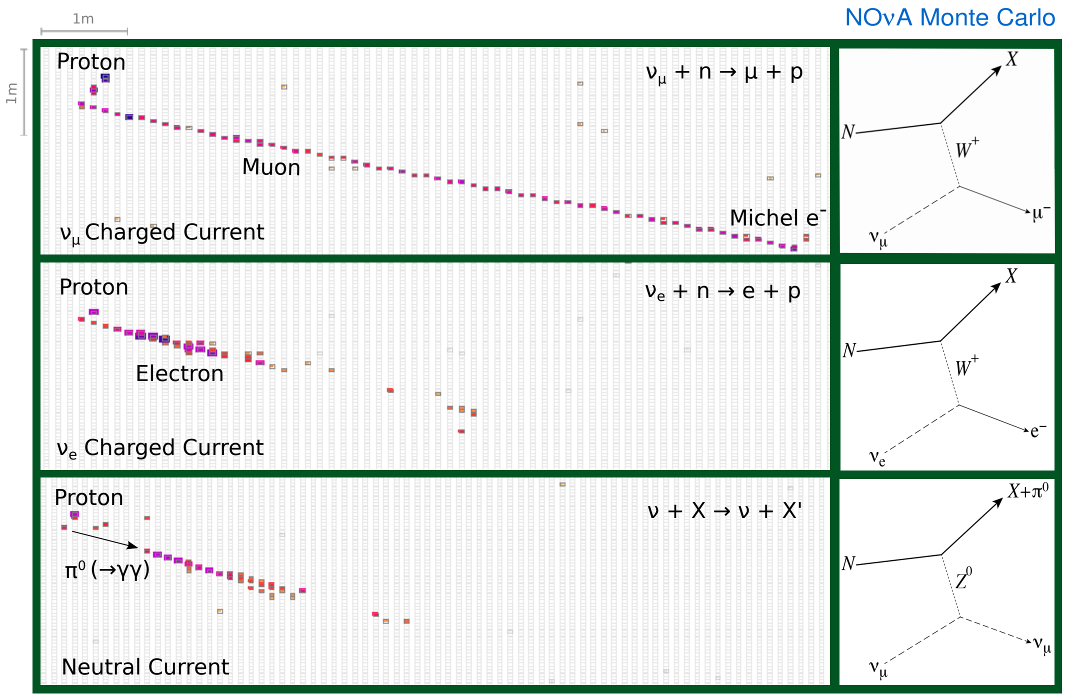

Figure 1.8: Different event topologies as seen in the NOvA detectors with corresponding Feynman diagrams [62]. Each event is a simulated 2.15 GeV neutrino interacting in a NOvA detector producing a 0.78 GeV proton and a second 1.86 GeV particle depending on the interactions type. The figure shows only one view and the colouring represents the deposited energy.

One of the ML algorithms that NOvA employs is a Convolutional Neural Network (CNN) based on the GoogLeNet [73] architecture named Convolutional Visual Network (CVN) [74]. When it is applied to identify entire events it is called *EventCVN* and uses slice hits to classify interactions into one of the five categories: ν_e, ν_μ, ν_τ, NC, or cosmic. The same architecture, but applied to the Fuzzy-K prongs, is called *ProngCVN* [75], and is used to identify what particles the prongs most likely correspond to. This assignment is useful in calculation of prong energy, as described in Sec. 1.7. Another ML algorithm is specifically designed for identifying muons and is based on a Boosted Decision Tree (BDT). It is called Reconstructed Muon Identifier (ReMId) [69] and uses the reconstructed Kalman tracks as inputs.

1.6 Detector Calibration

The energy deposited within NOvA detectors is represented by the peak ADC values for each cell the particle passed through, obtained from the readout electronics, as described in Sec. 1.3. The conversion of the peak ADC values into physical units of energy requires calibrating the NOvA detectors [76], while accounting for the attenuation of light along the WLS fibres, or for differences between individual cells. The purpose of calibration is to calculate a conversion factor from $\mathrm{ADC} \rightarrow \mathrm{MeV}$ for every part of the detector, so that the same energy deposited anywhere and at any time, is recorded as the same value of the reconstructed energy.

NOvA uses cosmic ray muons for calibration due to their abundance in the NOvA detectors and their consistent energy deposition. To calculate the absolute energy scale, NOvA selects a subsample of muons stopping inside of the detectors when they are almost exactly Minimum Ionising Particle (MIP) and therefore have a well understood energy deposition. The cosmic muons are collected using a periodic trigger with the same length as the beam trigger, whilst removing events with timestamps overlapping with the beam spill window. The simulation of cosmic muons is created using the CRY [60] MC generator, as outlined in Sec. 1.4.

Cosmic muon tracks are reconstructed using the window cosmic track algorithm described in Sec. 1.5. The selection of well reconstructed cosmic tracks requires that at least 80% of all hits from the reconstructed slice contribute to the track [29]. Each track must have at least 2 hits in both the x and y views and the difference in the number of planes the track crossed between the views must be at most 10% of the total number of planes. Also, the plane where each track starts or stops in one view must be within 3 planes of the start or stop plane in the other view. Additionally, since tracks that do not cross many planes tend to not be reconstructed very well, the extent of each track in the z direction must be at least $70\,\mathrm{cm}$ and tracks must have at least 20% of their total track direction in the z axis. Tracks with on average more than 6 cells per plane and with path lengths through the cell larger than $10\,\mathrm{cm}$ are removed for the same reason. Furthermore, all the reconstructed tracks must start at most $10\,\mathrm{cm}$ from the edge inside of the detector and stop at most $10\,\mathrm{cm}$ outside of the detector. Lastly, tracks with trajectory points far away from each other are also removed. The selection of stopping muons for the absolute energy scale relies on identifying Michel electrons, which are produced by decaying muons at the end of their tracks, as can be seen on the top panel of Fig. 1.8.

Since the energy deposited in a cell is proportional to the distance the particle travels through the cell, the input variable for calibration is the deposited energy divided by the path length through the cell PE/cm. To ensure the path length is well calculated, all hits used in calibration must satisfy the so-called 'tricell' condition, shown in Fig. 1.9. This means that for each calibration hit, there must be a corresponding hit in both of the surrounding cells in the same plane for the same track. The path length can then be calculated simply from the height of the cell and the angle of the reconstructed track. In case there is a bad channel in a neighbouring cell (right side of Fig. 1.9), this channel is ignored and the tricell condition looks one cell further [76]. If the tricell condition fails, the hit can still pass the 'z tricell' condition, which is a longitudinal equivalent of the tricell condition and requires a hit in both the neighbouring planes in the same view and with the same cell number. The 'z tricell' hits are saved separately and may be used if there are no hits satisfying the original tricell condition. This is especially useful for the cells on the edge of the detector, which fail the tricell condition due to only having one neighbouring cell.

The calibration conversion factor from the signal recorded by the detector readout to the deposited energy can be expressed by as

$$E_{dep}\ [\mathrm{MeV}] = \mathsf{Signal}\ [\mathrm{ADC}] \times S_d \times TS_{d,i}^{\textsc{Calib}} \times R_{d,i}\,(t) \times A_d\,(t)\,. \tag{1.1}$$

The calibration scale therefore consists of four separate and complementary factors: the Scale (S_d), the Threshold and Shielding correction $(TS_{d,i})$, the Relative calibration $(R_{d,i}\,(t))$ and the Absolute calibration $(A_d\,(t))$, all described below. Each part is

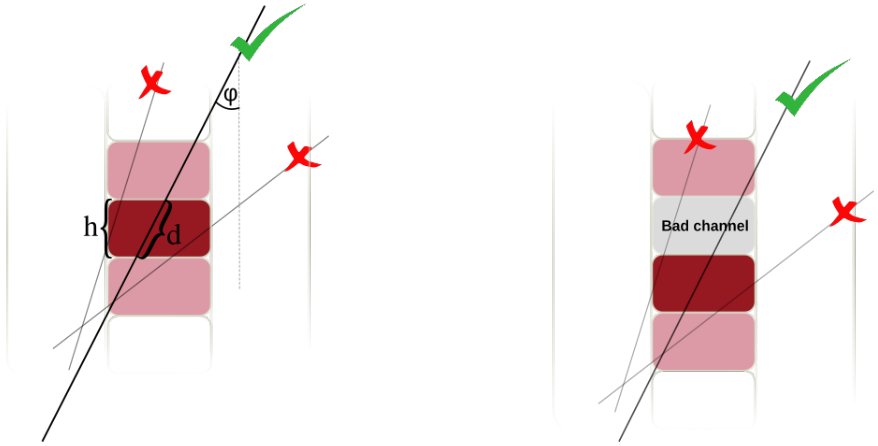

Figure 1.9: Illustration of the tricell condition. Only the hits with two surrounding hits in the same plane are used in the NOvA calibration, as shown on the left plot. This is to ensure a good quality of the path length (d) reconstruction, which is calculated from the known cell height (h) and the reconstructed track angle (φ). In case the hit is next to a bad channel, as shown on the right plot, the bad channel is ignored and the tricell condition requires a hit in the next cell over.

calculated for each detector separately, as indicated by the subscript d. The threshold and shielding correction is only used during calibration and is omitted when applying the calibration results. The relative and absolute calibrations are calculated for each time period separately to account for possible changes in the energy deposition throughout the time, possibly caused by the ageing of the scintillator oil, or of the readout electronics. The time periods are either determined by a fixed time interval, or by running conditions separated by significant changes to the readout or the DAQ systems, including the summer shutdown.

The threshold and shielding correction and the relative calibration calculate a calibration factor for each position within the detector to account for variations caused by the attenuation of light as it travels through the WLS fibres, or by differences between individual cells. This is expressed with a subscript i in Eq. 1.1. For data, the position of a hit in the detector is described by the plane number, cell number and the position within the cell (w). w is calculated as the projection of the cosmic track to the central cell axis and its value is equivalent to the x axis (y axis) coordinate of the projection for the horizontal (vertical) cells, with the 0 value at the centre of the cell [76].

For simulation, the calibration does not use the plane number to determine the position within a detector, as by construction all detector planes should have the same readout. This significantly reduces the requirements for the number of events that need to be simulated, reconstructed, and calibrated, especially for the FD with 896 planes. However, in reality there are some variations in the detector response between individual planes, caused by different *brightness* qualities of the fibres, zipped or twisted fibres, different qualities of the scintillator, possible air bubbles, and potentially other factors. To include these differences in simulation without having to simulate every cell individually, all the cells are divided into 12 equally populated Fibre Brightness (FB) bins based on the uncorrected average response in the center of that cell, as shown in Fig. 1.10. These FB bins describe the relative differences in the detector response between individual cells [77].

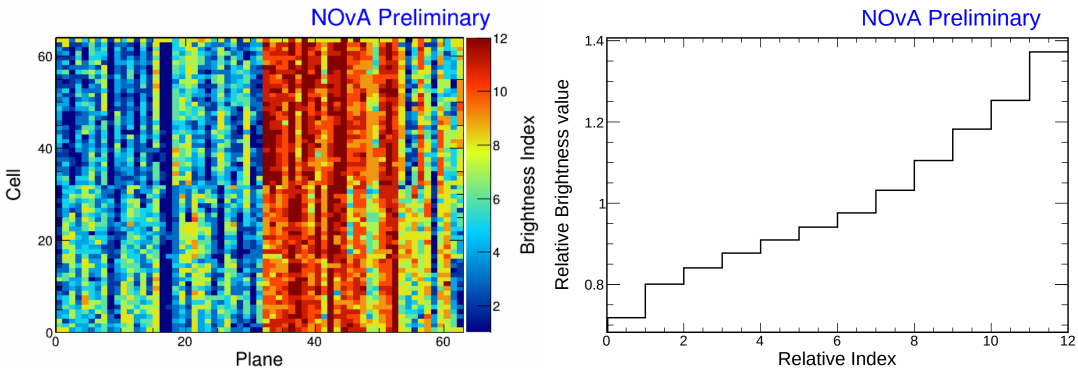

Figure 1.10: Distribution of the NOvA detector cells into 12 brightness bins (left plot), each representing a relative difference in energy response (right plot) due to different brightnesses of the fibres, scintillators, or readout. This is an example from the NOvA Test Beam detector, described in Sec. ??, where the left side of the detector (planes 1-32) has clearly lower response relative to the right side of the detector (planes 33-64).

1.6.1 Scale

The scale calibration factor from Eq. 1.1 is a simple conversion from the peak ADC value into the number of PEs. This factor only depends on the APD gain (which was different in the beginning of NOvA data taking) and on the FEB type (different between detectors, as described in Sec. 1.3).

1.6.2 Threshold and Shielding Correction

The threshold and shielding correction accounts for two assumptions, which hold true in most cases in NOvA, but fall short for some hits at the bottom of the detector, or far away from the readout, especially for the FD [76].

The first assumption is that the ADC response to the photon signal is linear, which is mostly true except close to the APD threshold. Energy deposited far away from the readout may produce photons that get attenuated enough to be shifted below the threshold. However, due to natural fluctuations of the number of photons created by the energy deposition, the same deposited energy may also produce photons that would make it over the threshold, therefore making it appear that the actual deposited energy was higher then in reality, introducing a bias to the calibration. The threshold correction is calculated using simulation, as the ratio between the mean of the Poisson distribution of the true number of the created PE ($\mathrm{PE}_{Poisson\lambda}$) and the number of the 'reconstructed' PE seen by the APD (PE_{Reco}).

The second assumption is that the spectrum of cosmic muons is uniform within each detector. Again, this is generally true, but breaks down in the FD, which is big enough for the top of the detector to shield the bottom of the detector and therefore affect the energy distribution. The shielding correction is calculated from simulation as a ratio between the expected deposited energy if the particle was a MIP (E_{MIP}), which is estimated from simulation for the NOvA scintillator as $E_{\mathrm{MIP}} = 1.78\,\mathrm{MeV/cm}$ and the true deposited energy (E_{true}).

The total threshold and shielding correction is calculated for simulated events in each cell, FB bin and w as

$$TS_i = \frac{\mathrm{PE}_{Poisson\lambda}}{\mathrm{PE}_{Reco}} \frac{E_{\mathrm{MIP}}}{E_{True}}. \tag{1.2}$$

To ensure that the correction changes smoothly across each cell position, the final correction is calculated as a fit to the mean correction value along w in each cell and FB bin.

1.6.3 Relative Calibration

The main goal of the relative calibration is to correct for the attenuation of the scintillator light as it travels through the WLS fibre to the readout. The attenuation in each cell is estimated by performing an 'attenuation fit' to the mean response in $\mathrm{PE/cm}$, as shown in Fig. 1.11. The relative calibration scale is then calculated as the ratio between the average response in $\mathrm{PE/cm}$ across the entire detector (can differ between

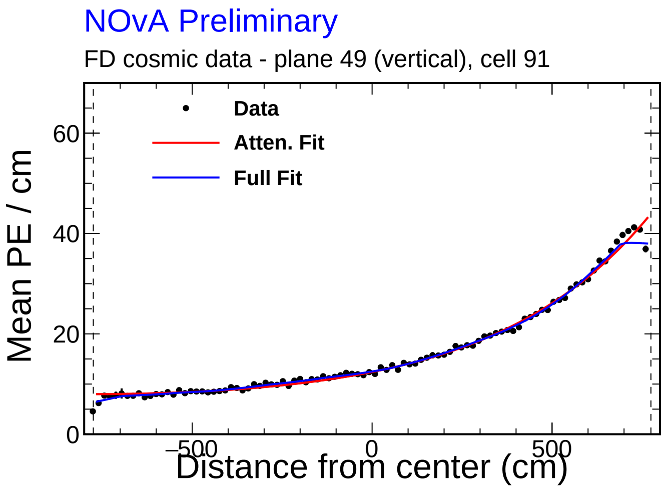

Figure 1.11: Example attenuation fit for a single cell in the NOvA FD across its full length, as shown by dashed vertical lines. The red line shows the initial exponential fit and the blue line shows the full fit after the LOWESS correction, both described in text. Figure from [78].

detectors) and the result of the attenuation fit in each particular position within the detector. The response after applying the relative calibration scale is expressed as Corrected Photo Electronss (PECorrs). Since the relative calibration scale is calculated for each cell independently, it effectively corrects for the relative differences between detector cells as well as for the attenuation. Therefore, the resulting distribution of PECorr/cm should be uniform across the detector, especially along the plane, cell and w [76].

The first step to do the attenuation fit is to create 'attenuation profiles' for each cell. Attenuation profiles are profile histograms of mean detector response over the path length through the cell, in the units of PE/cm, along the position within the cell. An example attenuation profile is shown in Fig. 1.11 as black dots. The threshold and shielding correction described in Sec. 1.6.2 is applied to the attenuation profiles before doing the attenuation fit, which consists of two steps.

1. The first step is a three-parameter exponential fit according to

$$y = C + A\left(\exp\left(\frac{w}{X}\right) + \exp\left(-\frac{L+w}{X}\right)\right), \tag{1.3}$$

where y is the fitted response, L is the length of the cell and C, A and X are the fitted parameters representing the background, attenuation scale and atten-

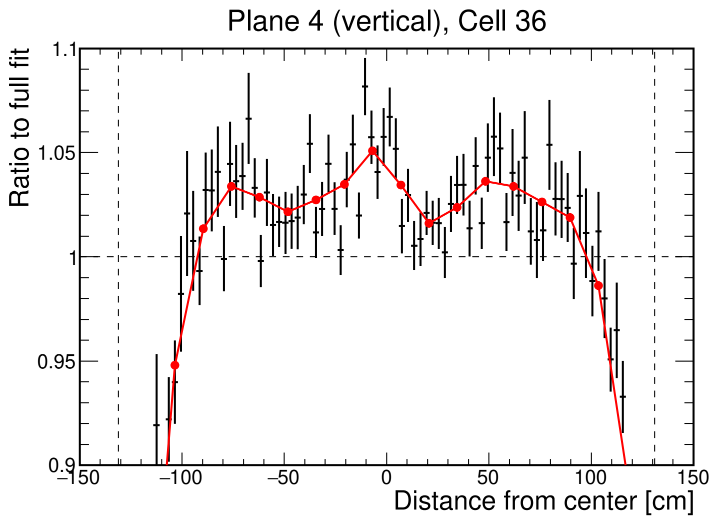

Figure 1.12: Example LOWESS correction for the residual differences after the exponential part of the attenuation fit of the NOvA relative calibration. This is an example for a single cell in the NOvA Test Beam detector with black points showing the residual differences and red line the LOWESS correction, both described in text.

uation length respectively. An example of the exponential fit is shown as a red curve in Fig. 1.11.

2. The second step is the smoothing out of residual differences between the exponential fit and the original distribution with the Locally Weighted Scatter plot Smoothing (LOWESS) method, shown in Fig. 1.12. The residual differences get evened out by creating a smooth distribution of 20 locally weighted points across the length of each cell. The result of the LOWESS correction is then combined with the exponential fit into the full attenuation fit, shown as a blue line in Fig. 1.11.

Even after applying the LOWESS correction, there are sometimes large differences between the attenuation fit and the fitted response. This is usually caused by a small number of events in that cell, common for cells at the edge of the detector. To ensure a good quality of the attenuation fit, the total χ^2 between the attenuation fit and the fitted response is calculated and only cells with the final $\chi^2 \leq 0.2$ are counted as *calibrated*. Cells with $\chi^2 > 0.2$ are ignored in further processing and marked as *uncalibrated*.

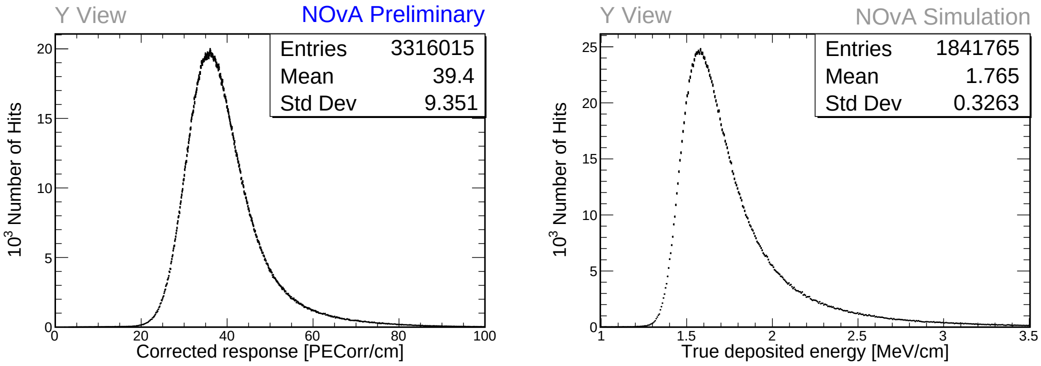

Figure 1.13: The absolute energy scale is calculated as the ratio between the simulated mean true deposited energy (right) and the mean reconstructed energy response (left) for selected stopping muons in each view and each data period or simulation.

1.6.4 Absolute Calibration

The absolute calibration only uses hits from muons stopping inside of the detector, in a track window $1-2\,\mathrm{m}$ from the end of their tracks. This is when they are approximately MIP and their energy deposition is well understood. Additionally, hits at the edges of each cell are removed to mitigate the effects at the end of the WLS fibres and the lower number of events at the edge of the detector [29].

First, the relative calibration results are applied to the selected stopping muon hits to get a distribution of the corrected detector response in $PECorr/\mathrm{cm}$, as shown on the left of Fig. 1.13. The mean of this distribution is called the *reconstructed* Muon Energy Unit (MEU) and is calculated separately in each of the two views, and in each time period or version of simulation. Analogously, the mean of the true deposited energy in $\mathrm{MeV/cm}$ from simulation, shown on the right of Fig. 1.13, is called the *true* MEU. The absolute energy scale (the absolute calibration scale) is then the ratio between the true and the reconstructed MEU value, where both the MEU values are taken as a simple average over the two views

$$\text{Absolute Energy Scale} = \frac{\mathrm{MEU}_{True}\ [\mathrm{MeV/cm}]}{\mathrm{MEU}_{Reco}\ [\mathrm{PE\textsc{Corr}/cm}]}. \tag{1.4}$$

The values of the absolute energy scales for each data period and simulation, as well as the results of the attenuation fit, are saved in a set of lookup tables, which are then used any time a hit is recorded in the NOvA detector and processed and reconstructed with the NOvA algorithms described above.

1.7 Energy Estimation

The deposited energy from detector calibration (Sec. 1.6) is only the first step in estimating the neutrino energy (E_ν) required for the main NOvA analyses.

For the ν_μ disappearance analysis, the ν_μ energy is measured as the sum of the muon energy and the energy of the hadronic shower [7]. The muon energy is identified from the length of its track, without the need of the calibration results. The energy of the hadronic shower is estimated from simulation as a fit to the 2D distribution of the true ν_μ energy minus the reconstructed muon energy, versus the visible (not corrected for the dead material) deposited energy of the hadronic system [75].

For the ν_e appearance analysis, the ν_e energy is calculated using a quartic fit to the 2D distribution of the electromagnetic versus the hadronic calorimetric energies, both corrected for the energy deposition in the dead material (PVC cells) [75]. The dead material correction is currently just a simple scaling of the deposited energy from calibration for all particles and is calculated from the measurement of the π^0 mass peak in the NOvA ND. This correction is correct only for electromagnetic showers and is not directly applicable to hadronic showers. The fit to determine the ν_e energy keeps the normalization of both the electromagnetic and the hadronic energies free, so the exact value of the dead material correction is not important. It is however used in other, non-neutrino oscillation analyses.

1.8 Systematic Uncertainties at NOvA

Systematic uncertainties in NOvA analyses arise from the imperfect knowledge on the individual components of the NOvA experiment, or from the known shortcomings of the prediction used to extract the measured parameters. Even though different analyses in NOvA need to consider different systematic uncertainties and their effect on the results varies, there are a few commonalities across all NOvA analyses that are explained below.

Both the 3-flavour [7] and the sterile neutrino [13] oscillation analyses in NOvA use the ND to constrain the FD prediction, which significantly reduces the effect of the neutrino beam and interaction prediction systematic uncertainties. On the other hand, these are the leading sources of systematic uncertainties for the ND-only analyses, such as the cross section analyses [8–11]. The leading systematic uncertainty for the neutrino oscillation measurements comes from the detector calibration uncertainty. Significant uncertainties for all NOvA measurements also come from the neutron modelling, the detector simulation and the muon energy estimation. There are other sources of systematic uncertainties that are not mentioned here as they are sub-dominant, or specific to a certain analysis.

The systematic uncertainty on the prediction of the neutrino beam consists of two parts: the hadron production and the beam focusing uncertainties [36]. The uncertainty for hadron production is estimated by the PPFX (describe in Sec. 1.4) using the multi-universe technique. Here we create 100 PPFX universes in which the inputs from the external measurements used to constrain the hadron production are randomly floated around their central values within their respective systematic uncertainties. Parts of the hadron production that are not constrained by external measurements are given a conservatively large systematic uncertainty. The beam focusing systematic uncertainties account for the uncertainties on the horn and target positions, the horn current, the beam position on the target, the beam spot size, and the effect of Earth's magnetic field in the beam pipe. TO DO: *Describe the beam PCA and how can we limit the beam uncertainty*

TO DO: *Describe the neutrino interaction modelling systematic uncertainties*

TO DO: *Describe the detector modelling systematic uncertainties*

TO DO: *Describe the neutron uncertainty - only if I decide I need it*

TO DO: *Describe the calibration uncertainties*

Chapter 2

Measuring the Muon Neutrino Magnetic Moment

What should I include here

- Objective of the study: State the goal of measuring the muon neutrino magnetic moment.
- Significance: Explain why this measurement is important in the context of particle physics.
- Brief background: Provide a short history of muon neutrino research and previous measurements.
  - Talk about Biao's measurement
  - LSND limit
  - XENONnT, LZ, XENON1T
  - Cosmology
- Overview of this chapter

In this analysis I am searching for a signal of possible effective muon neutrino magnetic moment events in the NOvA ND. This signal would manifest as an excess of neutrino-on-electron (ν-on-e) elastic scattering events at low electron recoil energies on top of the Standard Model (SM) background. In case there would be no discernible excess over the SM background, I would provide an upper limit on the value of the effective muon neutrino magnetic moment.

[Progression review 3] Measuring the neutrino magnetic moment would give us a strong hint towards the new physics Beyond Standard Model (BSM). If neutrinos are Dirac particles, their magnetic moment would be too small to measure in any current experiments (in most current BSM theories). However if neutrinos are Majorana particles, current experiments including NOvA and DUNE could be able to see its effect.

The most sensitive measurement of neutrino magnetic moment is the study of neutrinos elastically scattering off of electrons. If neutrino would have magnetic moment, it would add (without interference) a term to the ν-on-e elastic scattering cross section, which is quadratically dependent on the size of the effective magnetic moment and linearly dependent on the inverse of the electron recoil energy. The effective magnetic moment is related to the matrix elements of the dipole magnetic moment via the neutrino oscillation parameters and is different (but interconnected) for different neutrino flavours [3].

[Thesis readiness review] Neutrinos in theories beyond the Standard Model can obtain a measurable neutrino magnetic moment, which would manifest in the NOvA ND as an excess of ν-on-e elastics scattering interactions in low electron recoil energies. Measuring an enhanced neutrino magnetic moment would point towards the right BSM theory, inform us about the necessary energy scale of neutrino mass generation, or point towards neutrinos being Majorana particles.

[Progression review 3] The purity of the NuMI beam and the use of muon neutrinos and antineutrinos give NOvA a possibility to provide world leading measurement of the muon neutrino effective magnetic moment [8].

[Thesis readiness review] NOvA benefits from a near pure source of muon neutrinos and antineutrinos and should be able to provide a world leading limit on the muon neutrino magnetic moment.

[Progression review 3] Best limits [79] for this parameter come from the LSND experiment [80] at $\mu_{\nu_\mu} < 6.8 \times 10^{-10}\mu_B$ from more than 20 years ago.

[Progression review 3] The XENON1T experiment published a paper [81] in 2020 showing an excess of neutrino-on-electron events, which could correspond to an effective magnetic moment of solar neutrinos of $\mu_{\nu_\odot} \in (1.4, 2.9) \times 10^{-11}\mu_B$. This was later in 2022 disfavoured by the XENONnT [82] and the LUX-ZEPLIN [83] experiments, which provided strict constraints of $\mu_{\nu_\odot} < 0.64 \times 10^{-11}\mu_B$ and $\mu_{\nu_\odot} < 1.1 \times 10^{-11}\mu_B$ respectively. Given some basic assumptions [84, 85] this would correspond to more than an order of magnitude stricter limit on muon neutrino effective magnetic moment than NOvA could possibly deliver, but the relationship between effective magnetic moments of different neutrino flavours may be non-trivial (depends on the new physics introduced) and studying muon neutrinos remains an important endeavour [86].

[Progression review 3] Biao Wang already made a measurement of neutrino magnetic moment at the NOvA near detector for their thesis [87] and achieved a limit of $\mu_{\nu_\mu} < 1.58 \times 10^{-9} \mu_B$, however they didn't include a rigorous treatment of systematic uncertainties and their selection could've been considerably more advanced.

COMMENT: *Should I talk about the ND and LDM group's analyses since we're using their tools?* The ν-on-e interactions are also used in the ND group's analysis to constrain the neutrino beam prediction [88], which relies on the precise theoretical knowledge of the ν-on-e interaction cross section. They compare the total number of recorded ν-on-e interactions, with background subtracted based on a comparison of data and simulation in a sideband region, to the prediction. Since the number of ν-on-e events should only depend on the normalization of the neutrino beam, this analysis should give us a precise validation, or correction, of the neutrino flux normalization. There has been a large amount of work going into this analysis, including making special samples, weights, event classifiers, developing a dedicated event selection, or developing a background subtraction method, among others. To save time and analysis effort, we have taken most of these work at face value and applied it to the neutrino magnetic moment analysis. This will help us get the first good estimate of NOvA's capabilities to constraint (or measure) the neutrino magnetic moment.

The same detector signature of a single forward going electron shower, as present in the ν-on-e events, is also present in the Light Dark Matter (LDM) analysis [89]. This analysis is using a similar event selection to select the LDM events as the ND group, only without the final $E\theta^2$ cut (see Sec.**??**). However, instead of simply comparing the total event counts, the LDM analysis is using a CAFAna-based fitting framework to fit for the possible LDM signal in a distribution of electron recoil energy multiplied by electron recoil angle squared.

[Progression review 3] There is a broad group of analysers in the NOvA experiment who study the same neutrino-on-electron events to either provide a constraint on the neutrino beam systematic uncertainty [90], or to study light dark matter. These analysers developed special event resonctruction tools (such as specially trained neural networks), event selections, special enhanced samples, fitting frameworks and systematic uncertinty treatments. All these tools are directly transferable to my analysis and allow me to easily and rapidly provide a baseline version of the neutrino magnetic moment measurement.

In this chapter I will give an overview of the theory of neutrino electromagnetic interactions in Sec. 2.1 focusing on the effective neutrino magnetic moment and its implications to the ν-on-e measurements and other theoretical considerations. Then I will discuss the analysis strategy, as well as the data and simulation samples and the analysis weights in Sec. 2.2. Afterwards I will explain the signal and background definition and the selection of events for this analysis in Sec. 2.3, as well as the electron recoil energy and angle resolution studies and the choice of binning in Sec. 2.4. Then, I will talk about the systematic uncertainties present for this analysis and our efforts to mitigate them in Sec. 2.5 and the fitting framework chosen for this analysis in Sec. 2.6. Lastly I will explain the results of this analysis in Sec. 2.7 and discuss their implications in Sec. 2.8. Section 2.9 concludes the finding of this analysis.

TO DO: *Also check out NeutrinoMassesPheno2007.pdf, sec 6.4*

2.1 Theory of neutrino magnetic moment

As was describe in Sec. **??**, neutrinos in the SM are massless and electrically neutral particles. However, even SM neutrinos can have electromagnetic interaction through loop diagrams involving charged leptons and the W boson. These interactions are described by the neutrino charge radius, described in section 2.1.2 TO DO: *Re-write this since I'm not going to include the other elmag properties section* [91].

In general BSM theories, considering interactions with a single photon as shown on Fig. 2.1, neutrino electromagnetic interactions can be described by an *effective* interaction Hamiltonian [92]

$$\mathcal{H}_{em}^{(\nu)}(x) = \sum_{k,j=1}^{N} \overline{\nu}_k(x)\, \Lambda_\mu^{kj} \nu_j(x)\, A^\mu(x)\,. \tag{2.1}$$

Here $\nu_k(x)\,, k = 1, ..., N$, are neutrino fields in the mass basis with N neutrino mass states and x denotes the position. Λ_μ^{kj} is a general vertex function and $A^\mu(x)$ is the electromagnetic field.

The vertex function $\Lambda_\mu^{fi}(q)$ is generally a matrix and in the most general case

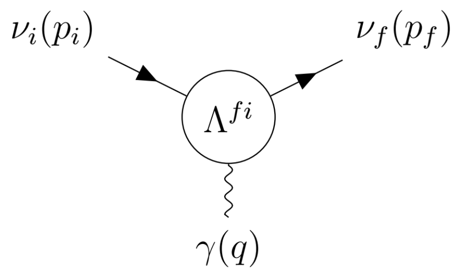

Figure 2.1: Effective coupling of neutrinos with one photon electromagnetic field.

consistent with the SM gauge invariance [93, 94] can be written in terms of linearly independent products of Dirac matrices (γ) and only depends on the four momentum of the photon ($q = p_f - p_i$):

$$\begin{aligned}\Lambda_\mu^{fi}(q) =& \mathbb{F}_1^{fi}\left(q^2\right) q_\mu + \mathbb{F}_2^{fi}\left(q^2\right) q_\mu \gamma_5 + \mathbb{F}_3^{fi}\left(q^2\right) \gamma_\mu + \mathbb{F}_4^{fi}\left(q^2\right) \gamma_\mu \gamma_5 + \\ & \mathbb{F}_5^{fi}\left(q^2\right) \sigma_{\mu\nu} q^\nu + \mathbb{F}_6^{fi}\left(q^2\right) \epsilon_{\mu\nu\rho\gamma} q^\nu \sigma^{\rho\gamma},\end{aligned} \tag{2.2}$$

where $\mathbb{F}_i^{fi}\left(q^2\right)$ are six Lorentz invariant form factors and δ and ϵ are the Dirac delta and the Levi-Civita symbols respectively.

Applying conditions of hermiticity $\left(\mathcal{H}_{em}^{(\nu)\dagger} = \mathcal{H}_{em}^{(\nu)}\right)$ and of the gauge invariance of the electromagnetic field, the vertex function can be rewritten as

$$\Lambda_\mu^{fi}(q) = \left(\gamma_\mu - q_\mu \not{q}/q^2\right)\left[\mathbb{F}_Q^{fi}\left(q^2\right) + \mathbb{F}_A^{fi}\left(q^2\right) q^2 \gamma_5\right] - i\sigma_{\mu\nu} q^\nu \left[\mathbb{F}_M^{fi}\left(q^2\right) + i\mathbb{F}_E^{fi}\left(q^2\right)\gamma_5\right], \tag{2.3}$$

where $\mathbb{F}_Q^{fi}, \mathbb{F}_M^{fi}, \mathbb{F}_E^{fi}$ and $\mathbb{F}_A^{fi}$ are hermitian matrices representing the charge, dipole magnetic, dipole electric and anapole neutrino form factors respectively. It is clear that the vertex function only depends on the square of the four momentum of the photon q^2. In coupling with a real photon ($q^2 = 0$) these form factors become the neutrino charge and magnetic, electric and anapole moments. The neutrino charge radius corresponds to the second term in the expansion of the charge form factor [92].

The above expression can be simplified as [95]

$$\Lambda_\mu^{fi}(q) = \gamma_\mu \left(Q_{\nu_{fi}} + \frac{q^2}{6}\langle r^2\rangle_{\nu_{fi}}\right) - i\sigma_{\mu\nu} q^\nu \mu_{\nu_{fi}}, \tag{2.4}$$

where $Q_{\nu_{fi}}$, $\langle r^2\rangle_{\nu_{fi}}$, and $\mu_{\nu_{fi}}$ are the neutrino charge, effective charge radius (also containing anapole moment), and an effective magnetic moment (also containing electric moment) respectively. This is possible thanks to the similar effect of the neutrino charge radius and the anapole moment, or of the neutrino magnetic and electric moment respectively [92]. These are the three neutrino electromagnetic properties (charge, charge radius and magnetic moment) measured in the experiments.

TO DO: *Add a note briefly describing the other elmag properties and mentioning that they could be measured as well, but not describe here. Maybe refer reader to the theoretical overview paper*

2.1.1 Neutrino electric and magnetic dipole moments

The size and effect of neutrino electromagnetic properties depend on the specific BSM theory. Evaluating the one loop diagrams in the minimally extended SM with three right-handed Dirac neutrinos as described in Sec. **??** gives the first approximation of the electric and magnetic moments:

$$\left.\begin{matrix} \mu_{kj}^{D} \\ i\epsilon_{kj}^{D} \end{matrix}\right\} \simeq \frac{3eG_F}{16\sqrt{2}\pi^2}(m_k \pm m_j)\left(\delta_{kj} - \frac{1}{2}\sum_{l=e,\mu,\tau} U_{lk}^{\star} U_{lj} \frac{m_l^2}{m_W^2}\right), \tag{2.5}$$

where m_k, m_j are the neutrino masses and m_l are the masses of charged leptons which appear in the loop diagrams [92]. Also, D superscript denotes Dirac neutrinos, e is the electron charge, G_F is the Fermi coupling constant, and U is the Pontecorvo-Maki-Nakagawa-Sakata (PMNS) neutrino oscillation matrix. Higher order electromagnetic corrections were neglected, but can also have a significant contribution, depending on the theory.

It can be seen that Dirac neutrinos have no diagonal electric moments $\left(\epsilon_{kk}^{D} = 0\right)$ and their diagonal magnetic moments are approximately

$$\mu_{kk}^{D} \simeq \frac{3eG_F m_k}{8\sqrt{2}\pi^2} \simeq 3.2 \times 10^{-19}\left(\frac{m_k}{\text{eV}}\right)\mu_B, \tag{2.6}$$

where μ_B is the Bohr magneton which represents the value of the electron magnetic moment [92]. Neutrino magnetic moments are therefore strongly suppressed by the smallness of neutrino masses, with theoretical predictions in Eq. 2.6 several orders of magnitude below the reach of current experiments [95].

The transition magnetic moments from Eq. 2.5 are suppressed with respect to the largest of the diagonal magnetic moments by at least a factor of 10^{-4} due to the m_W^2 in the denominator. The transition electric moments are even smaller due to the mass difference in Eq. 2.5. Therefore an experimental observation of a magnetic moment larger than in Eq. 2.6 would indicate physics beyond the minimally extended SM [92, 96].

TO DO: *Actually write why these values are different for Majorana neutrinos than for Dirac neutrinos* Majorana neutrinos in a minimal extension can be obtained by either adding a $\mathrm{SU}(2)_L$ Higgs triplet, or right handed neutrinos together with a $\mathrm{SU}(2)_L$ Higgs singlet [92]. If we neglect the Feynman diagrams which depend on the model of the scalar sector, the magnetic and electric dipole moments are

$$\mu_{kj}^M \simeq -\frac{3ieG_F}{16\sqrt{2}\pi^2}(m_k + m_j) \sum_{l=e,\mu,\tau} \mathrm{Im}\left[U_{lk}^\star U_{lj}\right] \frac{m_l^2}{m_W^2}, \tag{2.7}$$

$$\epsilon_{kj}^M \simeq \frac{3ieG_F}{16\sqrt{2}\pi^2}(m_k - m_j) \sum_{l=e,\mu,\tau} \mathrm{Re}\left[U_{lk}^\star U_{lj}\right] \frac{m_l^2}{m_W^2}. \tag{2.8}$$

These are difficult to compare to the Dirac case, due to possible presence of Majorana phases in the PMNS matrices, but it is clear that they have the same order of magnitude as Dirac transition dipole moments. However, the neglected model dependent contributions can enhance the transition dipole moments [92].

TO DO: *Re-read the natural upper bounds paper* It is possible [96] to obtain a 'natural' upper limits on the size of the neutrino magnetic moment by calculating its contribution to the neutrino mass by standard model radiative corrections. TO DO: *I don't think this is clear enough, how is this done* For Dirac neutrinos, the radiative correction induced by neutrino magnetic moment, generated at an energy scale Λ_{NP}, to the neutrino mass is generically

$$m_\nu^D \sim \frac{\mu_\nu^D}{3 \times 10^{-15}\mu_B}\left[\Lambda\,(\mathrm{TeV})\right]^2 \mathrm{eV}. \tag{2.9}$$

So for $\Lambda_{NP} \simeq 1\mathrm{TeV}$ and $m_\nu \lesssim 0.3\mathrm{eV}$ the limit becomes $\mu_\nu^D \lesssim 10^{-15}\mu_B$. This applies only if New Physics (NP) is well above the electroweak scale ($\Lambda_{EW} \sim 100\mathrm{GeV}$) TO DO: *Finish this sentence*. However, there are theories that contain a Dirac neutrino magnetic moment higher than this limit, for example in frameworks of minimal super-symmetric standard model, by adding more Higgs doublets, or by considering large extra dimensions TO DO: *Add references to the specific theories?* [92].

Similar limit for Majorana neutrino magnetic moment would be less stringent than for Dirac neutrinos due to the antisymmetry of the Majorana neutrino magnetic moment form factors TO DO: *Probably explain here a bit more what does this mean*. Considering $m_\nu \lesssim 0.3$eV, the limit can be expressed as

$$\mu_{\tau\mu}, \mu_{\tau e} \lesssim 10^{-9} \left[\Lambda\,(\mathsf{TeV})\right]^{-2} \tag{2.10}$$

$$\mu_{\mu e} \lesssim 3 \times 10^{-7} \left[\Lambda\,(\mathsf{TeV})\right]^{-2} \tag{2.11}$$

which is shown in the flavour basis TO DO: *Explain here what is the flavour basis*, which relates to the framework used previously via the PMNS matrix as

$$\mu_{ij} = \sum_{\alpha\beta} \mu_{\alpha\beta} U^\star_{\alpha i} U_{\beta j}, \quad \alpha, \beta \in \{e, \mu, \tau\}\,. \tag{2.12}$$

TO DO: *Add a discussion about the triangular inequalities*

These considerations imply, that if a magnetic moment $\mu \gtrsim 10^{-15}\mu_B$ would be measured, it is more plausible that neutrinos are Majorana fermions and that the scale of lepton violation would be well below the conventional see-saw scale [96] TO DO: *double check this claim, also reword this sentence*.

Effective neutrino magnetic moment

Since experiments detect neutrino flavour states, not the mass states, what we measure is an effective 'flavour' magnetic moment μ_{eff}. μ_{eff} is influenced by mixing of the neutrino magnetic moments (and electric moments) expressed in the mass basis (as described above) and neutrino oscillations TO DO: *This basis relation was already partly described above, mention that and combine the descriptions*. In the ultra-relativistic limit, the neutrino effective magnetic moment is

$$\mu^2_{\nu_l}\left(L, E_\nu\right) = \sum_j \left| \sum_k U^\star_{lk} e^{\mp i \Delta m^2_{kj} L/2E_\nu} \left(\mu_{jk} - i\epsilon_{jk}\right) \right|^2, \tag{2.13}$$

where the minus sign in the exponent is for neutrinos and the plus sign for antineutrinos [92]. Therefore the only difference between the effective neutrino and antineutrinos magnetic moment is in the phase induced by neutrino oscillations.

For experiments with baselines short enough that neutrino oscillations would not have time to develop ($\Delta m^2 L/2E_\nu \ll\sim 1$), such as the NOvA ND, the effective magnetic moment can be expressed as

$$\mu_{\nu_l}^2 = \mu_{\overline{\nu}_l}^2 \simeq \sum_j \left| \sum_k U_{lk}^\star \left(\mu_{jk} - i\epsilon_{jk}\right) \right|^2 = \left[U \left(\mu^2 + \epsilon^2\right) U^\dagger + 2\,\mathrm{Im}\left(U\mu\epsilon U^\dagger\right) \right]_{ll'} , \tag{2.14}$$

which is independent of the neutrino energy TO DO: *Figure out how does this relate to the mag moment cross section which does depend on the neutrino energy!*.

TO DO: *Consider if this paragraph is actually important* Since the effective magnetic moment depends on the flavour of the studied neutrino, it is different (but related) for neutrino experiments studying neutrinos from different sources. Additionally some experiments, namely solar neutrino experiments, need to include matter effects on the neutrino oscillations. Therefore the reports on the value (or upper limit) of the effective neutrino magnetic moment are not directly comparable between different types of neutrino experiments. Theorists publish papers trying to extrapolate the measured effective magnetic moments to each neutrino flavour, but necessarily apply assumptions that might not hold in all BSM theories.

2.1.2 Other neutrino electromagnetic properties

COMMENT: *I am not going to report results on these, so should I even mention them here? Maybe it's enough to just mention that they exist in the intro section...* TO DO: *This section is not finished, most of this text is just copied from some theory papers for now*

TO DO: *See also StatusAndPerspectiveOfNuMM2016.pdf*

Neutrino electric charge is heavily constraint by the measurements on the neutrality of matter (since generally neutrinos having an electric charge would also mean that neutrons have charge which would affect all heavier nuclei). It is also constrained by the SN1987A, since neutrino having an effective charge would lengthen its path through the extragalactic magnetic fields and would arrive on earth later. It can also be obtained from nu-on-e scatter from the relationship between neutrino millicharge and magnetic moment. [nuElmagInt2015.pdf - sec. VIIA] TO DO: *Make this descrip-*

tion shorter, just a single sentence and combine with the charge radius

The neutrino charge radius is determined by the second term in the expansion of the neutrino charge form factor and can be interpreted using the Fourier transform of a spherically symmetric charge distribution. It can also be negative since the charge density is not a positively defined quantity. In the SM the charge radius has the form of (possible other definitions exist)

$$\langle r^2_{\nu_l} \rangle_{\mathsf{SM}} = \frac{G_{\mathsf{F}}}{4\sqrt{2}\pi^2} \left[3 - 2 \log \left(\frac{m_l^2}{m_W^2} \right) \right]. \tag{2.15}$$

This corresponds to $\langle r^2_{\nu_\mu} \rangle_{\mathsf{SM}} = 2.4 \times 10^{-33}\ \mathrm{cm}^2$ and similar scale for other neutrino flavours. [nuElmagInt2015.pdf - sec. VIIB]

[nuElmagInt2015.pdf - sec. VIIB] The effect of the neutrino charge radius on the neutrino-on-electron scattering cross section is through the following shift of the vector coupling constant (Grau and Grifols, 1986; Degrassi, Sirlin, and VMarciano, 1989; Vogel and Engel, 1989; Hagiwara et al., 1994):

$$g_V^{\nu_l} \to g_V^{\nu_l} + \frac{2}{3} m_W^2 \langle r^2_{\nu_l} \rangle \sin^2 \theta_W \tag{2.16}$$

[nuElmagInt2015.pdf - sec. VIIB] The current experimental limits for muon neutrinos are from TO DO: *check the current exp. limits* Hirsch, Nardi, and Restrepo (2003) who obtained the following 90% C.L. bounds on $\langle r^2_{\nu_\mu} \rangle$ from a reanalysis of CHARM-II (Vilain et al., 1995) and CCFR (McFarland et al.,1998) data:

$$-0.52 \times 10^{-32} < \langle r^2_{\nu_\mu} \rangle < 0.68 \times 10^{-32}\ \mathrm{cm}^2 \tag{2.17}$$

In the Standard Model, the neutrino anapole moment is somehow coupled with the neutrino charge radii and is functionally identical. the phenomenology of neutrino anapole moments is similar to that of neutrino charge radii. Hence, the limits on the neutrino charge radii discussed in Sec. VII.B also apply to the neutrino anapole moments multiplied by 6. in the standard model the neutrino charge radius and the anapole moment are not defined separately and one can interpret arbitrarily the charge form factor as a charge radius or as an anapole moment. Therefore, the standard model values for the neutrino charge radii in Eqs. (7.35)–(7.38) can be interpreted also as values of the corresponding neutrino anapole moments. [nuElmagInt2015.pdf - sec. VIIC]

It is possible to consider the toroidal dipole moment as a characteristic of the neutrino which is more convenient and transparent than the anapole moment for the description of T-invariant interactions with nonconservation of the P and C symmetries. the toroidal and anapole moments coincide in the static limit when the masses of the initial and final neutrino states are equal to each other. The toroidal (anapole) interactions of a Majorana as well as a Dirac neutrino are expected to contribute to the total cross section of neutrino elastic scattering off electrons, quarks, and nuclei. Because of the fact that the toroidal (anapole) interactions contribute to the helicity preserving part of the scattering of neutrinos on electrons, quarks, and nuclei, its contributions to cross sections are similar to those of the neutrino charge radius. In principle, these contributions can be probed and information about toroidal moments can be extracted in low-energy scattering experiments in the future. Different effects of the neutrino toroidal moment are discussed by Ginzburg and Tsytovich (1985), Bukina, Dubovik, and Kuznetsov (1998a, 1998b), and Dubovik and Kuznetsov (1998). In particular, it has been shown that the neutrino toroidal electromagnetic interactions can produce Cherenkov radiation of neutrinos propagating in a medium. [nuElmagInt2015.pdf - sec. VIIC]

2.1.3 Measuring neutrino magnetic moment

The most sensitive method to measure neutrino magnetic moment is the low energy elastic scattering of (anti)neutrinos on electrons [92]. The diagram for this interaction is shown in Fig. 2.2 displaying the two observables, the recoil electron's kinetic energy $(T_e = E_{e\prime} - m_e)$ and the recoil angle with respect to the incoming neutrino beam (θ).

COMMENT: *Is this derivation too trivial to mention in a thesis? Should I just mention the results? I wanted to have this in the technote, but probably too detailed for a thesis...* TO DO: *Also change all we to passive voice - or should I keep we here?* From simple $2 \to 2$ kinematics we can calculate

$$(P_\nu - P_{e'})^2 = (P_{\nu'} - P_e)^2 \,, \tag{2.18}$$

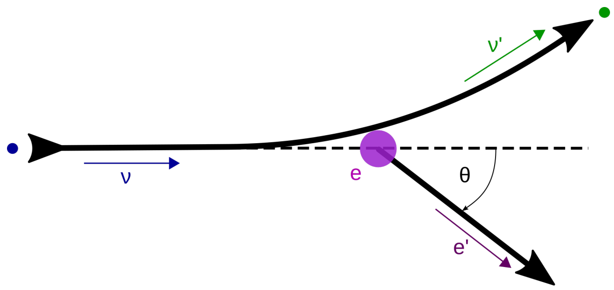

Figure 2.2: Neutrino-on-electron elastic scattering diagram

$$m_\nu^2 + m_e^2 - 2E_\nu E_{e'} + 2E_\nu p_{e'} \cos\theta = m_\nu^2 + m_e^2 - 2E_{\nu'} m_e. \tag{2.19}$$

Using the energy conservation

$$E_\nu + m_e = E_{\nu'} + E_{e'} = E_{\nu'} + T_e + m_e \Rightarrow E_{\nu'} = E_\nu - T_e \tag{2.20}$$

we get

$$E_\nu p_{e'} \cos\theta = E_\nu E_{e'} - E_{\nu'} m_e = E_\nu \left(T_e + m_e\right) - \left(E_\nu - T_e\right) m_e = T_e \left(E_\nu + m_e\right), \tag{2.21}$$

$$\cos\theta = \frac{E_\nu + m_e}{E_\nu} \sqrt{\frac{T_e^2}{E_{e'}^2 - m_e^2}} = \frac{E_\nu + m_e}{E_\nu} \sqrt{\frac{T_e^2}{T_e^2 + 2T_e m_e}}. \tag{2.22}$$

And finally we get

$$\cos\theta = \frac{E_\nu + m_e}{E_\nu} \sqrt{\frac{T_e}{T_e + 2m_e}}. \tag{2.23}$$

We can rearrange the Eq. 2.23 to get

$$T_e = \frac{2m_e E_\nu^2 \cos^2\theta}{\left(E_\nu + m_e\right)^2 - E_\nu^2 \cos^2\theta}. \tag{2.24}$$

Electron's kinetic energy is therefore kinematically constrained by the energy conservation as

$$T_e \leq \frac{2E_\nu^2}{2E_\nu + m_e}, \tag{2.25}$$

which corresponds to the $\cos\theta \to 1$ when the recoil electron goes exactly forward in the incident neutrino direction.

Considering $E_\nu \sim$ GeV, we can approximate $\frac{m_e^2}{E_\nu^2} \to 0$ and from Fig.2.3 we can see that we can approximate all recoil angles to be very small, therefore $\theta^2 \cong (1 - \cos^2\theta)$.

Using Eq.2.23 we get

$$T_e\theta^2 \cong T_e\left(1-\left(\frac{E_\nu+m_e}{E_\nu}\right)^2\frac{T_e}{T_e+2m_e}\right) = T_e\left(1-\left(1+\frac{2m_e}{E_\nu}\right)\frac{T_e}{T_e+2m_e}\right), \tag{2.26}$$

therefore

$$T_e\theta^2 \cong \frac{2m_eT_e}{T_e+2m_e}\left(1-\frac{T_e}{E_\nu}\right) = 2m_e\left(\frac{1}{1+\frac{2m_e}{T_e}}\right)\left(1-\frac{T_e}{E_\nu}\right), \tag{2.27}$$

and finally

$$T_e\theta^2 \cong 2m_e\left(1-\frac{T_e}{E_\nu}\right) < 2m_e. \tag{2.28}$$

This is a strong limit that clearly distinguishes the ν-on-e elastic scattering events from other similar interaction involving single electron (mainly the ν_eCC interaction).

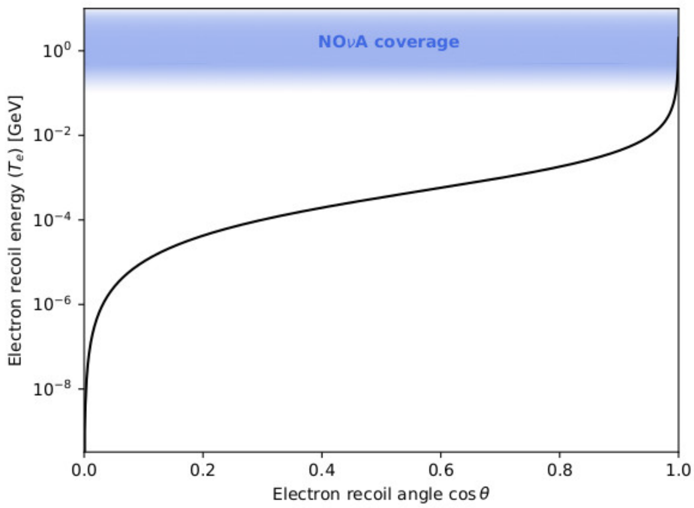

Figure 2.3: Relation between the recoil electron's kinetic energy and angle for ν-on-e elastic scattering. The coverage of the NOvA detectors for measuring the electron recoil energy is shown in blue. Only very forwards electron's are recorded in NOvA.

Neutrino magnetic moment cross section

COMMENT: *Should this only be a subsubsection?* In the ultra-relativistic limit, the neutrino magnetic moment changes the neutrino helicity, turning active neutrinos into sterile TO DO: *cite this properly*. Since the SM weak interaction conserves helicity we can simply add the two contribution to the ν-on-e cross section incoherently [92]:

$$\frac{d\sigma_{\nu_l e^-}}{dT_e} = \left(\frac{d\sigma_{\nu_l e^-}}{dT_e}\right)_{\text{SM}} + \left(\frac{d\sigma_{\nu_l e^-}}{dT_e}\right)_{\text{MAG}}. \tag{2.29}$$

The SM contribution can be expressed as [92]:

$$\left(\frac{d\sigma_{\nu_l e^-}}{dT_e}\right)_{\text{SM}} = \frac{G_F^2 m_e}{2\pi}\left\{(g_V^{\nu_l}+g_A^{\nu_l})^2 + (g_V^{\nu_l}-g_A^{\nu_l})^2\left(1-\frac{T_e}{E_\nu}\right)^2 + \left((g_A^{\nu_l})^2-(g_V^{\nu_l})^2\right)\frac{m_e T_e}{E_\nu^2}\right\}, \tag{2.30}$$

where the coupling constants g_V and g_A are different for different neutrino flavours and for antineutrinos. Their values are:

$$g_V^{\nu_e} = 2\sin^2\theta_W + 1/2, \qquad g_A^{\nu_e} = 1/2, \tag{2.31}$$

$$g_V^{\nu_{\mu,\tau}} = 2\sin^2\theta_W - 1/2, \qquad g_A^{\nu_{\mu,\tau}} = -1/2. \tag{2.32}$$

For antineutrinos $g_A \to -g_A$.

TO DO: *Decide if this is actually useful or not* Using Eq. 2.24 it is possible to get the differential cross section for $\cos\theta$:

$$dT_e = \frac{4m_e E_\nu^2 (m_e+E_\nu)^2}{\left[(m_e+E_\nu)^2 - E_\nu^2\cos^2\theta\right]^2}\cos\theta d\cos\theta \tag{2.33}$$

as

$$\left(\frac{d\sigma_{\nu_l e^-}}{d\cos\theta}\right)_{\text{SM}} = \frac{2G_F^2 E_\nu^2 m_e^2 \cos\theta\,(E_\nu+m_e)^2}{\pi\left((E_\nu+m_e)^2 - E_\nu^2\cos^2\theta\right)^2} \left\{(g_V^{\nu_l}+g_A^{\nu_l})^2 + (g_V^{\nu_l}-g_A^{\nu_l})^2\left(1-\frac{2m_e E_\nu\cos^2\theta}{(E_\nu+m_e)^2-E_\nu^2\cos^2\theta}\right)^2 + \left((g_A^{\nu_l})^2-(g_V^{\nu_l})^2\right)\frac{2m_e^2\cos^2\theta}{\left((E_\nu+m_e)^2-E_\nu^2\cos^2\theta\right)}\right\}, \tag{2.34}$$

The neutrino magnetic moment contribution is TO DO: *include derivation from [?]* [92]:

$$\left(\frac{d\sigma_{\nu_l e^-}}{dT_e}\right)_{\text{MAG}} = \frac{\pi\alpha^2}{m_e^2}\left(\frac{1}{T_e}-\frac{1}{E_\nu}\right)\left(\frac{\mu_{\nu_l}}{\mu_B}\right)^2, \tag{2.35}$$

ht

Table 2.1: Neutrino-on-electron elastic scattering total cross sections. TO DO: *Move units to title and add cross sections with thresholds. Also reference this somewhere in text* from Fundamentals of neutrino Physics and Astrophysics, p.139

Process	Total cross section
$\nu_e + e^-$	$\simeq 93 \times 10^{-43} E_\nu \mathrm{cm}^2\mathrm{GeV}^{-1}$
$\overline{\nu}_e + e^-$	$\simeq 39 \times 10^{-43} E_\nu \, \mathrm{cm}^2\mathrm{GeV}^{-1}$
$\nu_{\mu,\tau} + e^-$	$\simeq 15 \times 10^{-43} E_\nu \, \mathrm{cm}^2\mathrm{GeV}^{-1}$
$\overline{\nu}_{\mu,\tau} + e^-$	$\simeq 13 \times 10^{-43} E_\nu \, \mathrm{cm}^2\mathrm{GeV}^{-1}$

where α is the fine structure constant TO DO: *Calculate the total mag moment cross sections*.

Comparison of the SM and the neutrino magnetic moment cross sections is shown on Fig.2.4. Whereas the SM cross section is flat with $T_e \to 0$, the neutrino magnetic moment cross section keeps increasing to infinity. However, this reach is limited by the experimental capabilities of detecting such low energetic neutrinos. Possible NOvA coverage is shown in a shaded blue and it is uncertain we could actually reach as low as 100 MeV TO DO: *Change this claims a little bit*.

As can be seen in Fig. 2.4 and Fig. 2.5, the magnetic moment contribution exceeds the SM contribution for low enough T_e. This can be approximated as [92]:

$$T_e \lesssim \frac{\pi^2\alpha^2}{G_F^2 m_e^3}\left(\frac{\mu_\nu}{\mu_B}\right)^2 \simeq 2.9 \times 10^{19}\left(\frac{\mu_\nu}{\mu_B}\right)^2 [\mathrm{MeV}]\,, \tag{2.36}$$

which does not depend on the neutrino energy and makes experiments sensitive to lower energetic electrons more sensitive to the neutrino magnetic moment. This is especially true for the recent dark matter experiments which put stringent limits on the solar neutrino effective magnetic moment, as described in the following section.

2.2 Analysis overview

What should be included here:

- Data collection - Explain how data is collected, including the duration and conditions of data taking. Talk about possible RHC data and future data?
- Event Reconstruction
- Simulation

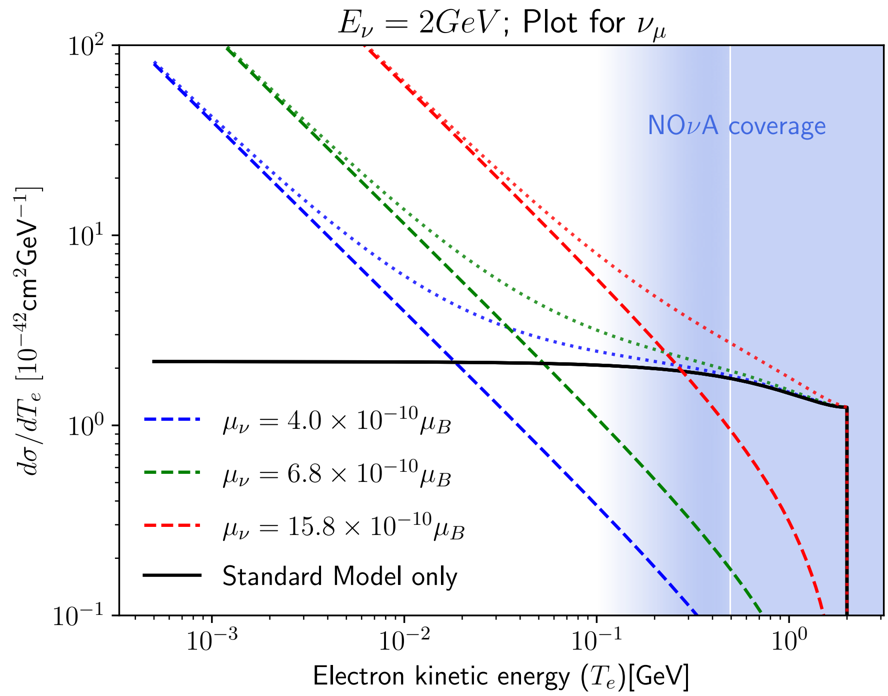

Figure 2.4: Comparison of the neutrino magnetic moment (coloured) and the SM (black) cross sections for the ν-on-e elastic scattering. Different colours depict different values of the neutrino magnetic moment. Dashed lines are the individual cross sections and dotted lines are the added total cross section with the standard model contribution. NOvA coverage of electron recoil energies is shown in shaded blue TO DO: *Reference the colours on the figures to the origins of the values (LSND and Biao)*.

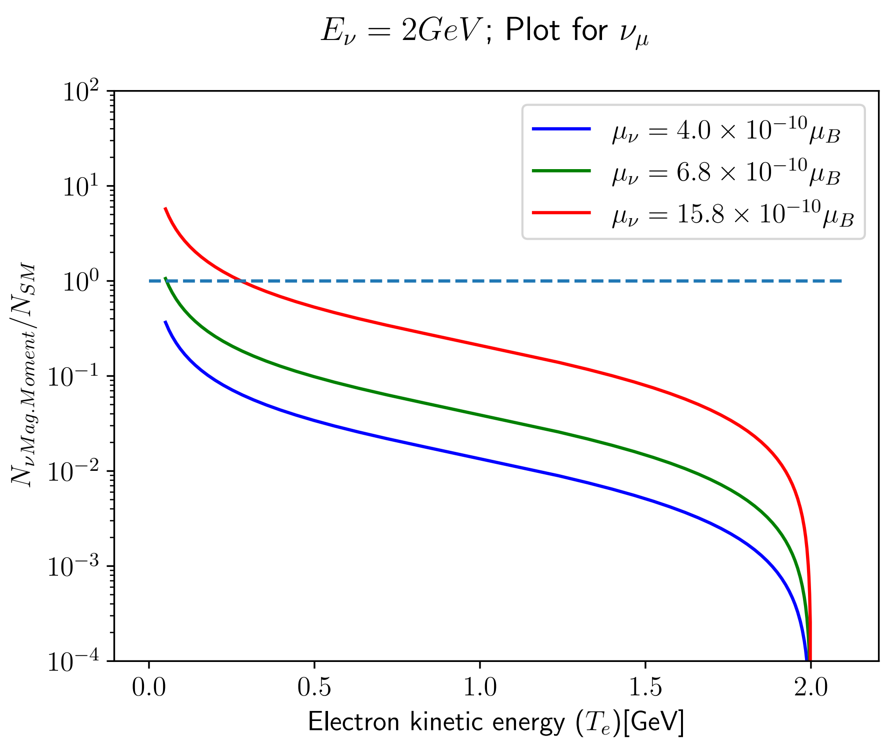

Figure 2.5: Ratio of the neutrino magnetic moment cross section to the SM cross section for the ν-on-e elastic scattering. Different colours depict different effective muon neutrino magnetic moment values.

  - Nominal ND
  - Enhanced nuone
  - Enhanced nueccMEC

- Weights
  - Overview
  - PPFX and XSec weights
  - Radcorr weight
  - Magnetic moment signal as a weight

Our analysis strategy is to compare the count of the recorded neutrino events in data with the prediction. We are considering two hypotheses. Under the null hypothesis, which assumes no effective muon magnetic moment, the predicted number of events corresponds to the simulation true ν-on-e events under the SM processes. For the alternative hypothesis, the predicted number of signal events, which depends on the value of the effective neutrino magnetic moment, and appear on top of the SM background from the null hypothesis.

COMMENT: *Should I maybe discuss the statistical analysis used already here?*

The data used in this analysis was collected from the start of the NOvA ND data taking on the 22nd of August 2014, until the 3rd of February 2021. This is the same ND data as was used in the latest NOvA neutrino oscillations result [7], with a additional one year of data taking. NOvA collected more data until the writing of this thesis, this data is however still being processed and it is not available at the time of writing this thesis. The full ND-equivalent exposure of the data sample is approximately 13.8×10^{20} POT. This exposure is used to scale all the predictions in this chapter to properly compare the predicted number of events to the expectations in data.

We are using the standard NOvA simulation and reconstruction tools as were discussed in Sec. **??** and 1.5. The simulation was created with approximately $4\times$ larger number of events than in data to limit statistical uncertainties from simulation. The total exposure for the simulation is approximately 55.4×10^{20} POT. For the studies of the systematic uncertainties, only a smaller portion of this is used, specifically 19.3×10^{20} POT exposure.

To tackle the low number of ν-on-e and ν_eCC MEC events in the nominal simulation sample we are using a suit of nominal and enhanced simulation samples for four different signal and background components. Each one contains its nominal sample and special systematically shifted samples for the detector systematics. The use of the samples is summarised in table **??** and described in detail below.

Created by Wenjie Wu (was it just him or also Yiwen?) to do ... and fully described in the technote [88]. Using the overlayed and filematched samples for consistency. Correct POT is 1.72e+24 (this should be filematched). missing cross section parameters to save on file size

[ND group's technote] Because the cross section of the nuone elastic scattering is very low (approx. 1/2000 of the total charged-current cross section), the statistics of nuone elastic scattering is not enough in the inclusive sample. In order to optimize the signal selection criteria, we made a sample with only nuone elastic scattering events in the detector. The size of this nuone signal MC is 1.48E23 POT. However the pile-up of neutrino interactions in one spill impacts on the hit clustering in reconstruction, either hits from the nuone elastic scattering can be clustered to other interactions or extra hits can be clustered to the nuone elastic scattering.

Created by Yiwen Xiao [88] to tackle the low statistics of the ν_eCC MEC background events and subsequently large and unphysical cross section weights. Correct POT is 1.99e+24 (filematched). There are limitations of the sample in the q3-q0 parameter space.

TO DO: *Describe already here the signal definitions, but only very briefly, basically just need to say that the signal also includes true vertex contained in the detector*

TO DO: *Describe here that we're using the nominal ND MC sample for signal utilizing the simple relationship between the Standard Model cross section and the neutrino magnetic moment cross section (ref. theory)*

The signal of the neutrino magnetic moment analysis is just a re-weighted signal of the ν-on-e analysis from the near detector group. We are using the same event selection as the near detector group.

The signature of the neutrino magnetic moment is a single very forward low energetic electron shower. The major backgrounds are NC and ν_μCC interactions that produce π^0 in the final state, which decays into two γ, mimicking the signal.

NOvA is not super well suited for a low energy detection and there are troubles identifying very low energetic event. Majority of the analyses in NOvA only use events with energies above $0.5\,\mathrm{GeV}$. nueCCXSec only uses events above 1 GeV. The numuCCpi0 XSec ana had a low E cutoff at 0.1GeV

2.2.1 Analysis weights

TO DO: *Describe why do we use weights* What are the weights we are using and why? weights used to correct for known limitations of the simulation

To correct for known deficiencies in simulation of neutrino flux or cross sections we apply weights calculated for each event.

[ND group's technote] In order to ensure that the Monte Carlo used in this analysis is representative of the most up-to-date knowledge of both cross sections and flux, weights were applied to each simulated event based on true event information.

PPFX weight

[?] TO DO: *What does this do (one sentence ish).* Maybe cite Leo's thesis? Or paper? L. Aliaga, "Neutrino Flux Prediction for the NuMI Beamline." PhD Thesis, FERMILAB-1081 THESIS-2016-03

[ND group's technote] The flux weight reweights the flux to the central value prediction, based on external hadron production measurements, from the PPFX package

Prod5.1 GSF XSec weight

TO DO: *Find the reference: possibly Maria's docdb:53336 together with the official 2020 XSec tuning technote docdb:43962.*

NOvAReweight reference: J. Wolcott, "NOvARwgt software." https://github.com/novaexperiment/N public.

TO DO: *Briefly describe what does this do. Also mention Yiwen's talk/technote about the large XSec weights that made her create an enhanced nueCC MEC sample.*

We are only using the for the background since we assume that the cross section for the signal is perfect. Also there are not weights for this kind of interaction.

[ND group's technote] The cross-section weight is a combination of different weights applied to various processes. The major effects of this weight are

- Adjust the axial mass (MA) for CCQE cross section to $1.04\,\mathrm{GeV/c^2}$ based on the error-weighted mean of updated ANL, BNL, and FNAL experiments.
- Applies the empirical MEC weight determined from the cross section tuning fit.
- Reduces non-resonant single pion production by 50%.
- Applies RPA suppression that models nuclear screen effects at low values Q2 to QE and RES interactions.
- Reduces GENIE predicted DIS events with $W > 1.7\,\mathrm{GeV}$ by 10%.

Radiative correction weight

TO DO: *Why are we doing this? (reference Yiwen's talk/technote).*

Mention here where did I get the original GENIE cross section from (reference Yiwen's talk or technote, plus the original paper that was used). nu-on-e technote[88]

TO DO: *Write out the actual version of the weight. Including the original and the corrected XSec constants*

MINERvA paper: https://journals.aps.org/prd/pdf/10.1103/PhysRevD.100.092001

Say that we are not using the third part of the correction because it is tiny and it makes no difference. (tried and tested)

[ND group's technote] In GENIE, the cross section of the nuone elastic scattering signal is calculated at the tree level. To improve the precision of the simulated nuone elastic scattering cross section, we performed radiative corrections to the GENIE nuone elastic scattering as shown in Appendix A.

TO DO: *correct the equation* Calculated as

$$weight_{\text{Radiative Corr.}} = \left.\frac{d\sigma_{\nu-on-e}}{dy}\right|_{\text{Radiative Corr.}} / \left.\frac{\mathrm{d}\sigma_{\nu-on-e}}{\mathrm{d}y}\right|_{\text{GENIE 3}} ;\, y = \frac{E_e - m_e}{E_\nu} \tag{2.37}$$

Neutrino magnetic moment signal as a weight

TO DO: *What does this do and why does it work? Reference the theory part as to why is the magnetic moment signal simply a rescaling of the GENIE cross section.*

Using the same tree-level cross section from GENIE as in the rad. corr. weight.

TO DO: *Write the name of the weight in CAFAna/nuone namespace and where it is located*

TO DO: *correct the equation* Calculated as

$$weight_{\nu \text{ Mag. Moment}} = \left.\frac{d\sigma_{\nu-on-e}}{dy}\right|_{\nu \text{ Mag. Moment}} / \left.\frac{\mathrm{d}\sigma_{\nu-on-e}}{\mathrm{d}y}\right|_{\text{GENIE 3}} ;\, y = \frac{E_e - m_e}{E_\nu} \tag{2.38}$$

The summary of the simulation samples and analysis weights for the three different types of signal and background component is shown in Tab. 2.2.

2.3 Event selection

Introduction: We are searching for ν-on-e events at low electron recoil energies. Due to their small cross section compared to other processes, there is only a limited number of ν-on-e events that can be utilized. Therefore, we are focusing on retaining as

Table 2.2: Overview of the simulation samples and analysis weight used for the different signal and background components.

Signal type	Sample	Weight
Signal	Enhanced ν-on-e	Flux & ν Mag. Moment
ν-on-e background	Enhanced ν-on-e	Flux & Rad. Corr.
ν_eCC MEC background	Enhanced ν_eCC MEC	Flux & Cross Sec.
Other background	Nominal ND	Flux & Cross Sec.

many events as possible, while reducing the background. There are a few notable features that can be utilized to select low energetic ν-on-e events. Specifically that ν-on-e events are characterized by a single very forward going electromagnetic shower.

We are trying to select low energy neutrino-on-electron events, which are characterised by a single very forward going electron shower. This is a similar task to the ND group and to the ν_e appearance search for the three flavour group.

The main background in NOvA in general are the ν_μCC events. They are generally easy to identify from our signal, however their sheer number makes them a dominant background nevertheless. Additionally, there are backgrounds that have the same or similar topology to our signal. These are specifically the ν_eCC events that produce electrons. Additionally, there are interactions that produce π^0, which can look similar to our signal in our detector. These can be from either ν_μ or ν_e, and can be both CC or NC.

We explain the motivation behind each cut of the event selection and discuss their effect on the neutrino magnetic moment events below. We also consider possible improvements to the event selection for a future (re-)analysis.

Should I describe already here the electron reconstruction and therefore resolution? The plots for energy resolution are done using full selection... The only place it comes into play for us (single bin analysis) is through the cuts involving energy

The strategy for event selection is as follows. First, we remove misreconstructed and untrusted events. Then we apply pre-selection cuts that remove obvious background, by limiting the reduction of the signal efficiency at most at $0.2\,\%$. Then we apply the containment cuts that remove events that are either not fully contained within the detector, or events that originate from outside of the detector, such are rock muons. Then we look at a selection of variables inside a TMVA and choose the cuts that are give us the best signal over background ratio. Given that we have a very limited number of signal events, our chosen Figure Of Merit (FOM) is a simple

$$\mathsf{FOM} = \frac{\mathsf{Signal}}{\sqrt{\mathsf{Background}}}. \tag{2.39}$$

Data Collection Quality

Spill cuts To ensure good data quality, we apply the following criteria on the run, subrun and spill level. TO DO: *Add a description of the spill quality cuts (only applied to data)*

COMMENT: *How much in detail do I need to go in here? This is very technical. Should I even include this? See 3fl technote for more detail*

Reconstruction Quality

Since electron are reconstructed by slicing, then vertexing, then reconstructing prongs. To identify electron we request that there is a valid reconstructed vertex and at least one reconstructed prong. Even though electrons only consist of a single shower, we don't reject events with more than one prongs in a slice, as the reconstruction can wrongly assign noise hits as a separate prong. We do not want to reject these events as we might still recover the true signal event from there.

TO DO: *Discuss why so many events do not have a reconstructed vertex*

Additionally, we're placing a cut on the number of hits per plane to < 5. This is to remove the so-called 'FEB flashers', which are caused by a very high energy deposit in one cell, such that it affects all the other channel on the same APD [97]

Literally taken from the 3 flavour's nue appearance low energy selection Pre-selection cuts include basic quality cuts that remove events with invalid vertex reconstruction and events with no reconstructed prongs, as shown on Fig. **??**.

[nueXSec ana, docdb:37668] One additional detector issues is the presence of "FEB Flashers" within reconstructed slices. FEB flashers are caused by high energy deposits in one cell, which induces a sagged baseline in all other channels on the same APD. When the baseline is restored, fake hits are triggered on the whole APD.

Requiring at least one reconstructed vertex and at least one reconstructed prong (and shower). Also requiring that there are < 8 hits per plane to remove FEB flashers.

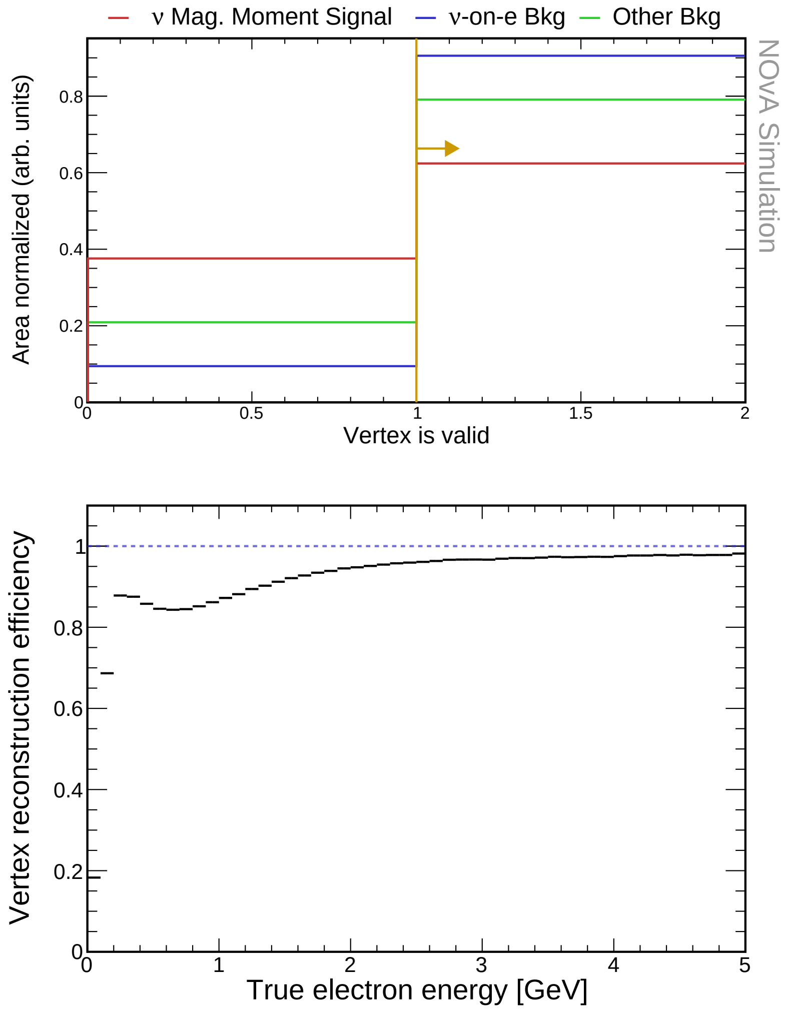

Figure 2.6: Relative comparison of signal, ν-on-e background, and other background events for basic reconstruction quality selection variables. No cuts were applied to make these plots. Yellow lines indicate the cut values for the shown variables, with arrows pointing towards the preserved events. All plots show relative comparison with histograms normalised to their areas.

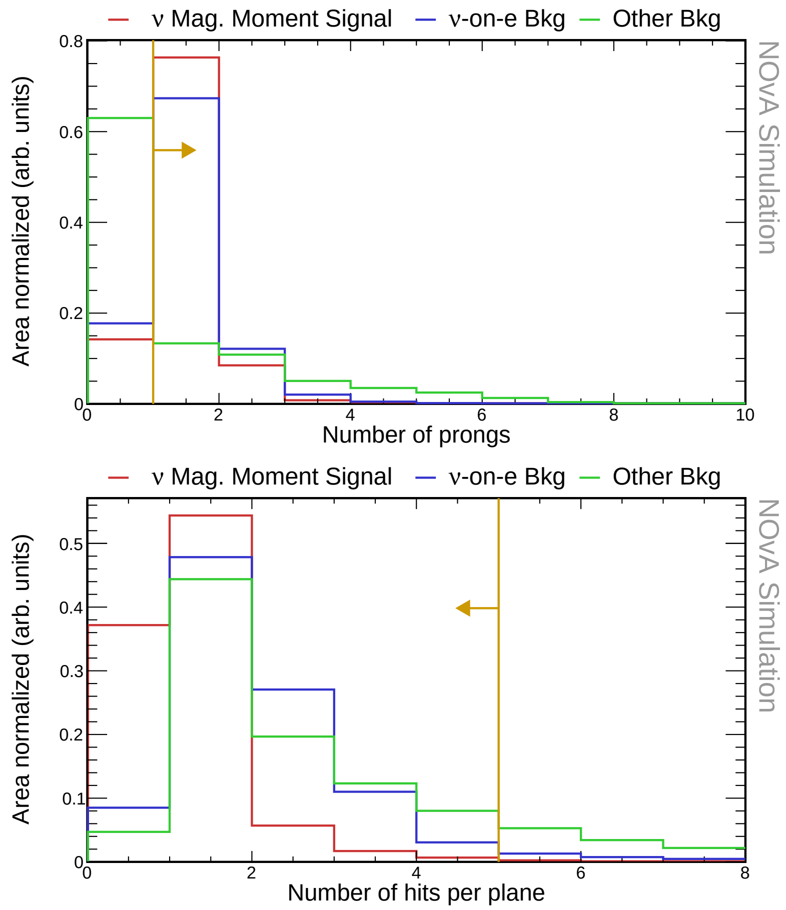

Figure 2.7: Relative comparison of signal, ν-on-e background, and other background events for basic reconstruction quality selection variables. No cuts were applied to make these plots. Yellow lines indicate the cut values for the shown variables, with arrows pointing towards the preserved events. All plots show relative comparison with histograms normalised to their areas.

Shower energy cut

COMMENT: *Already applying the cut here to help reduce the events for TMVA. This cut is based purely on reco quality (we don't trust events below 0.5GeV, especially not for the CVN nuone ID variables0*

TO DO: *discuss the energy cut, should this be removed? What is the effect on the event count? Why was this included in the first place (the identifiers are not as strong for lower energies - is this true though? - also there are further unexplored backgrounds that would need to be further studied and explore. Maybe depends on where would we move the cut...)* The calorimetric energy of the primary shower is required to be $E_{cal} > 0.5\,\mathrm{GeV}$.

Basic Event Selection

again Literally taken from the 3 flavour's nue appearance low energy selection - variables, not the values.

The cut values for the basic event selection were chosen so that they cut out most of the background, while only approximately $0.2\,\%$ of signal events

The criterion for these cuts will be that each of them has to limit the signal efficiency by 0.25% or lower. This means that in total the preselection cuts will lower the signal efficiency by 1% or lower, which is acceptable.

The pre-selection cuts have been kept from the ν_eCC analysis with loosened cut values TO DO: *find a reference for this analysis*. They also remove the obvious ν_μCC interactions by requiring that the length of the longest prong is < 500 cm and the summed number of cells for all prongs in the slice is < 200. Relative comparison of signal, ν-on-e background, and other background distributions for the pre-selection variables is shown on Fig. **??**. This is much stricted than the ND group's $NHits < 600$, $LongestPlane < 800\mathrm{cm}$ and planes crossed by the longest prong < 120.

Table 2.3: Event selection cutflow table

Selection	**Signal**		**ν-on-e bkg**		**Other bkg**	
	N_{evt}	ϵ^{N-1} (%)	N_{evt}	ϵ^{N-1} (%)	N_{evt}	ϵ^{N-1} (%)
No Cut	269.76	100	3.43×10^3	100	2.96×10^8	100
Valid Vtx	180.54	66.93	3.33×10^3	96.94	2.34×10^8	79.10
N Prongs	174.65	96.74	64.74×10^3	96.99	8.66×10^7	37.01
Hits / Plane	-	-	-	-	-	-

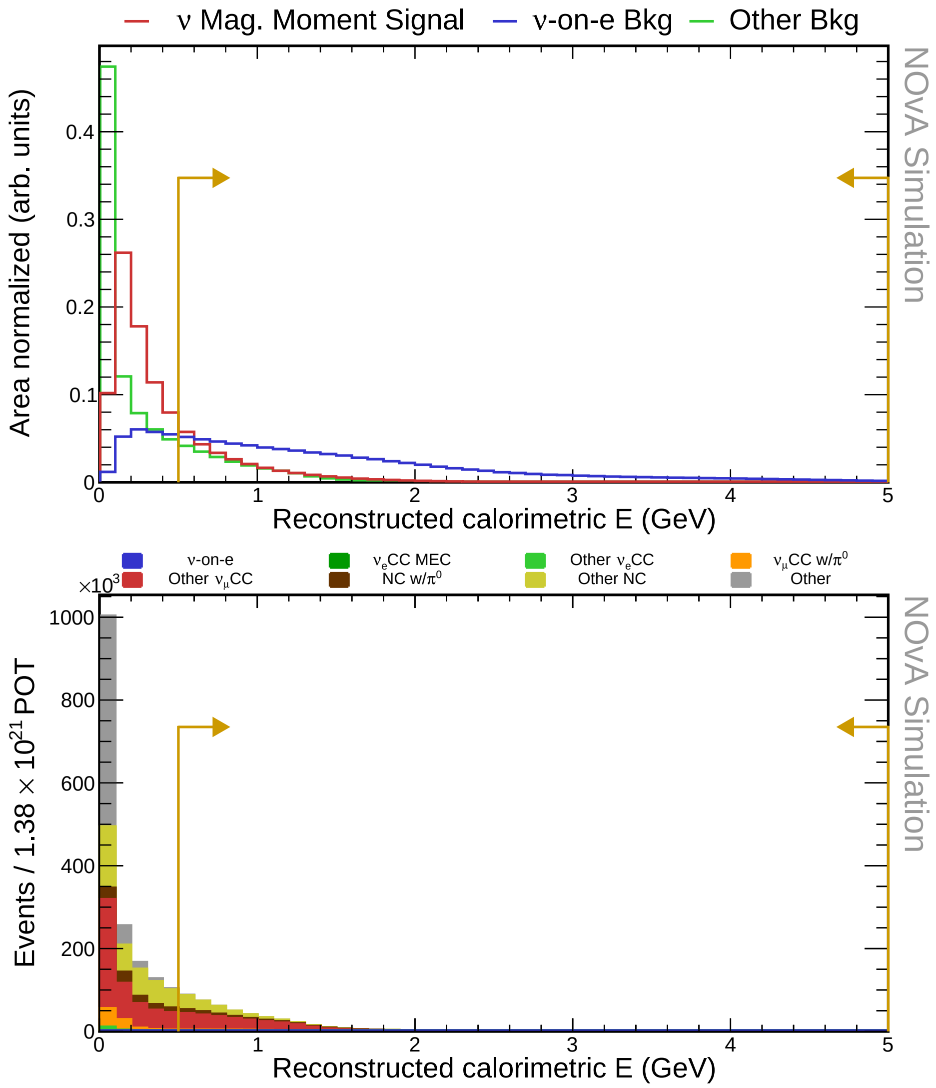

Figure 2.8: Relative comparison of signal, ν-on-e background, and other background events for the reconstructed vertex. No cuts were applied to make these plots. Gold lines show the cut values that create the fiducial volume.

TO DO: *Mention that I added a preliminary $E\theta^2 < 0.04$ cut*

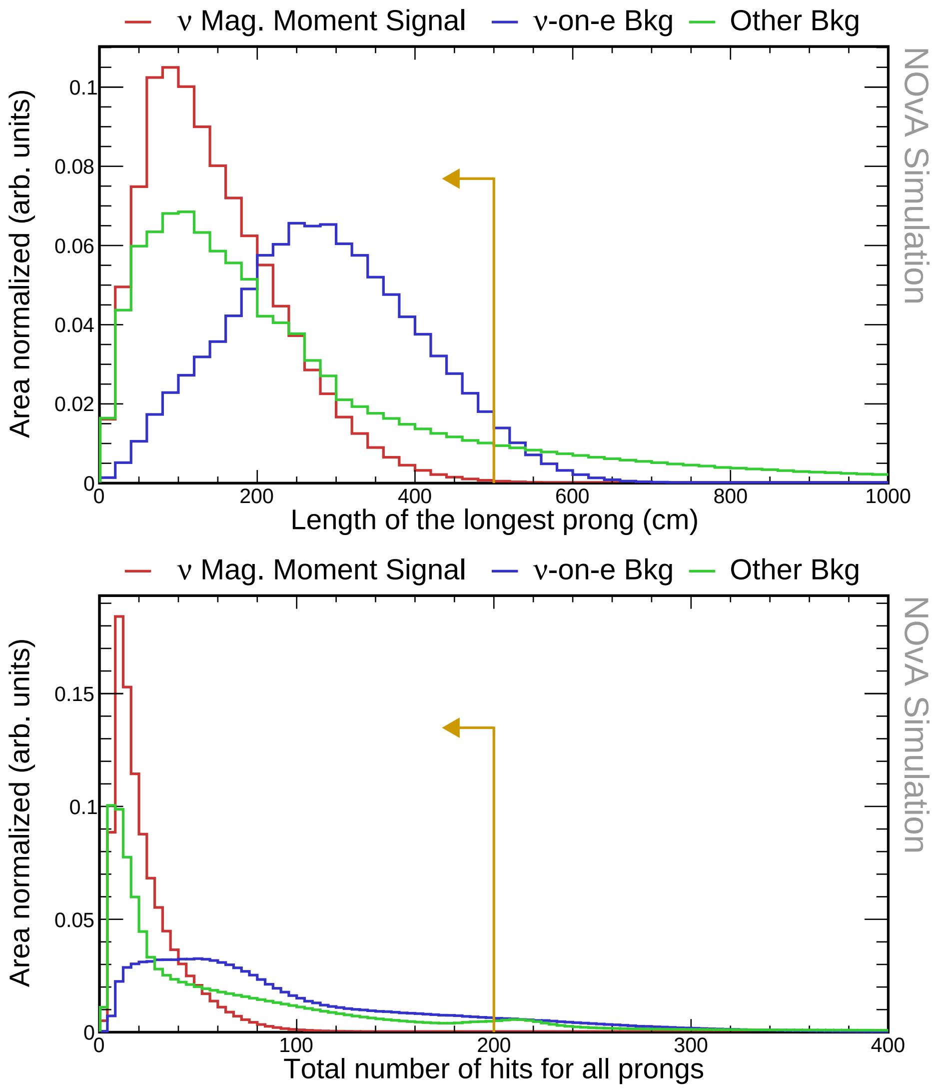

Figure 2.9: Relative comparison of signal, ν-on-e background, and other background events for basic pre-selection variables. Cuts on VtxIsValid, number of prongs, and number of hits per plane were applied to make these plots. Yellow lines show the cut values for the shown variables.

Fiducial and containment cuts

[nueXSec ana, docdb:37668] For both the X and Y vertices the distributions are asymmetric when comparing across the origin, in terms of vertex position. This is primarily due to particles coming from the +y and -x from events in the rock surrounding the detector. This corresponds to the direction of the NuMI target from the near detector. ...We require all activity from neutrino activity be deposited outside of the muon catcher.

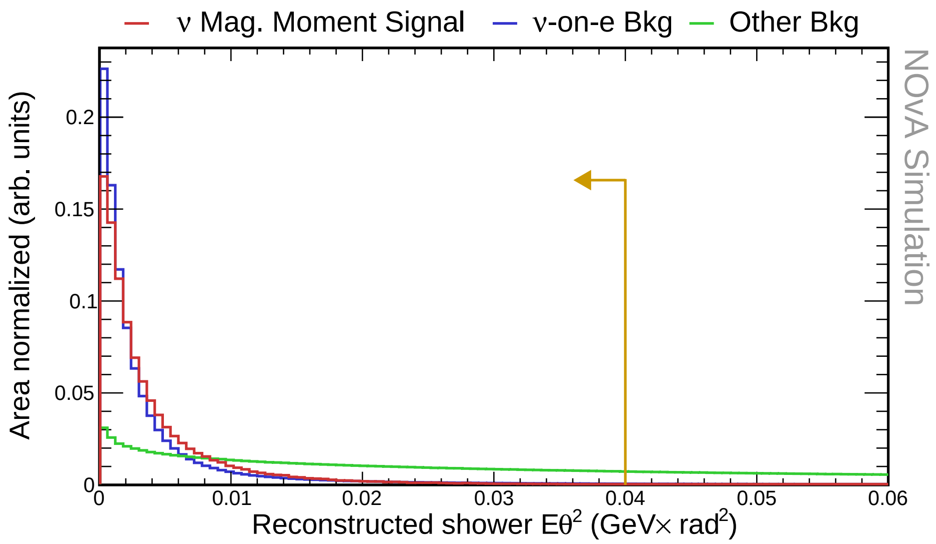

Figure 2.10: Relative comparison of signal, ν-on-e background, and other background events for basic pre-selection variables. Cuts on VtxIsValid, number of prongs, and number of hits per plane were applied to make these plots. Yellow lines show the cut values for the shown variables.

TO DO: *Describe what does the fiducial cut do* We require that the reconstructed vertex is contained within the following volume: $-175 < \mathsf{Vtx}_X < 175, -175 < \mathsf{Vtx}_Y < 175, 95 < \mathsf{Vtx}_Z < 1095$ cm.

To ensure all the energy is contained within the detector and to remove events originating outside of the detector (rock muons), we require that the extreme positions of hits for all prongs in the slice are within the following volume: $-175 < \mathsf{min}_X, \mathsf{max}_X < 175, -175 < \mathsf{min}_Y, \mathsf{max}_Y < 175, 105 < \mathsf{min}_Z, \mathsf{max}_Z < 1270$ cm. COMMENT: *Also made this a bit stricter from the ND group's values as it didn't really make sense*

Single particle requirement

COMMENT: *This is where I started the TMVA*

To selection events with a single particle we require that the fraction of energy contained in the most energetic shower is > 0.8, that the summed energy of all cells (above threshold and within ± 8 planes from the vertex) outside of the most energetic shower is < 0.02 GeV, and that the distance between the vertex and the start of the primary shower is < 20 cm.

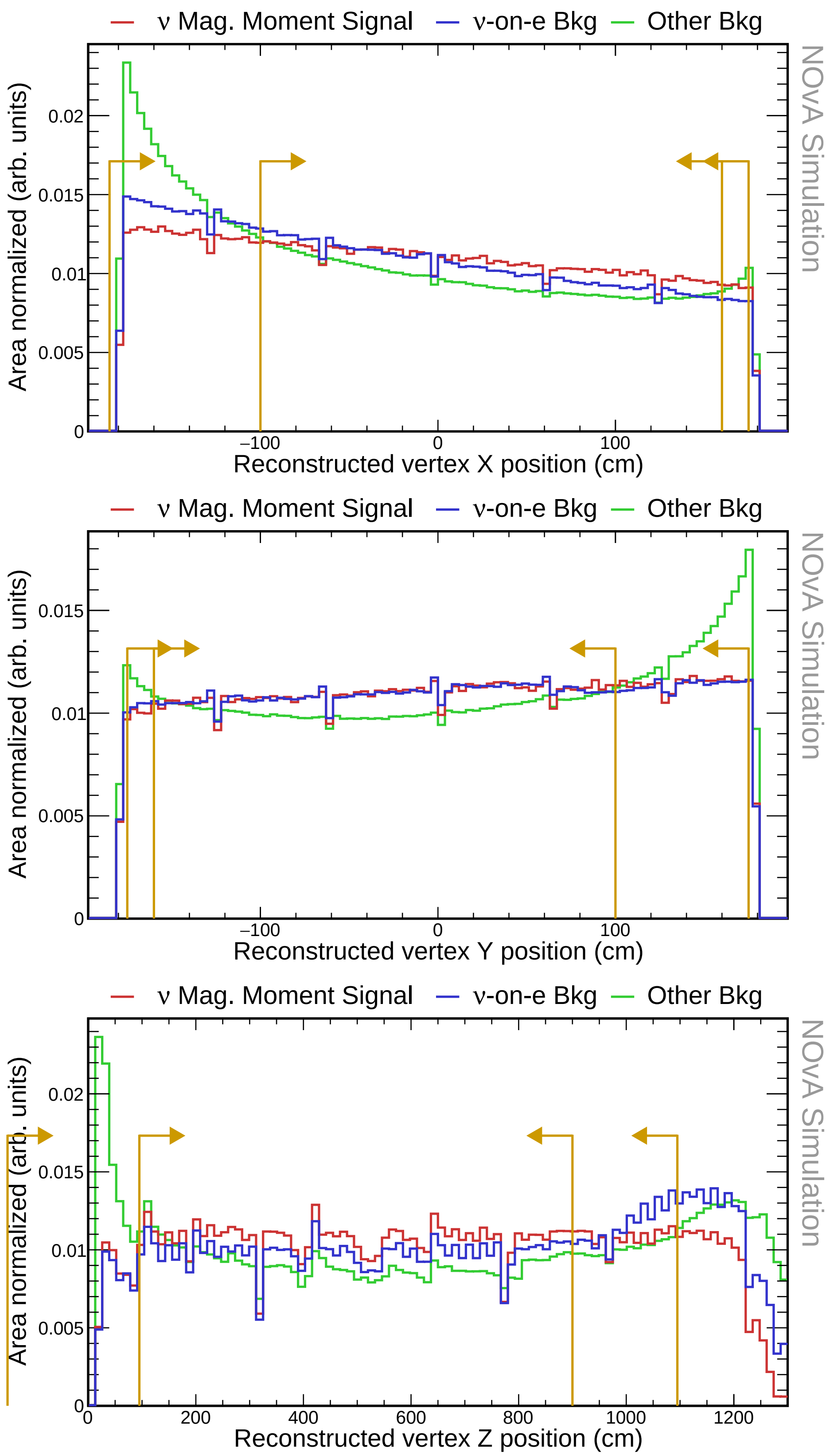

Figure 2.11: Relative comparison of signal, ν-on-e background, and other background events for the reconstructed vertex. Basic reconstruction quality and pre-selection cuts were applied prior to making these plots. Additionally, vertex is required to be within the active region of the detector ($< 1270\,\mathrm{cm}$) for the two top plots. Gold lines show the cut values that create the fiducial volume.

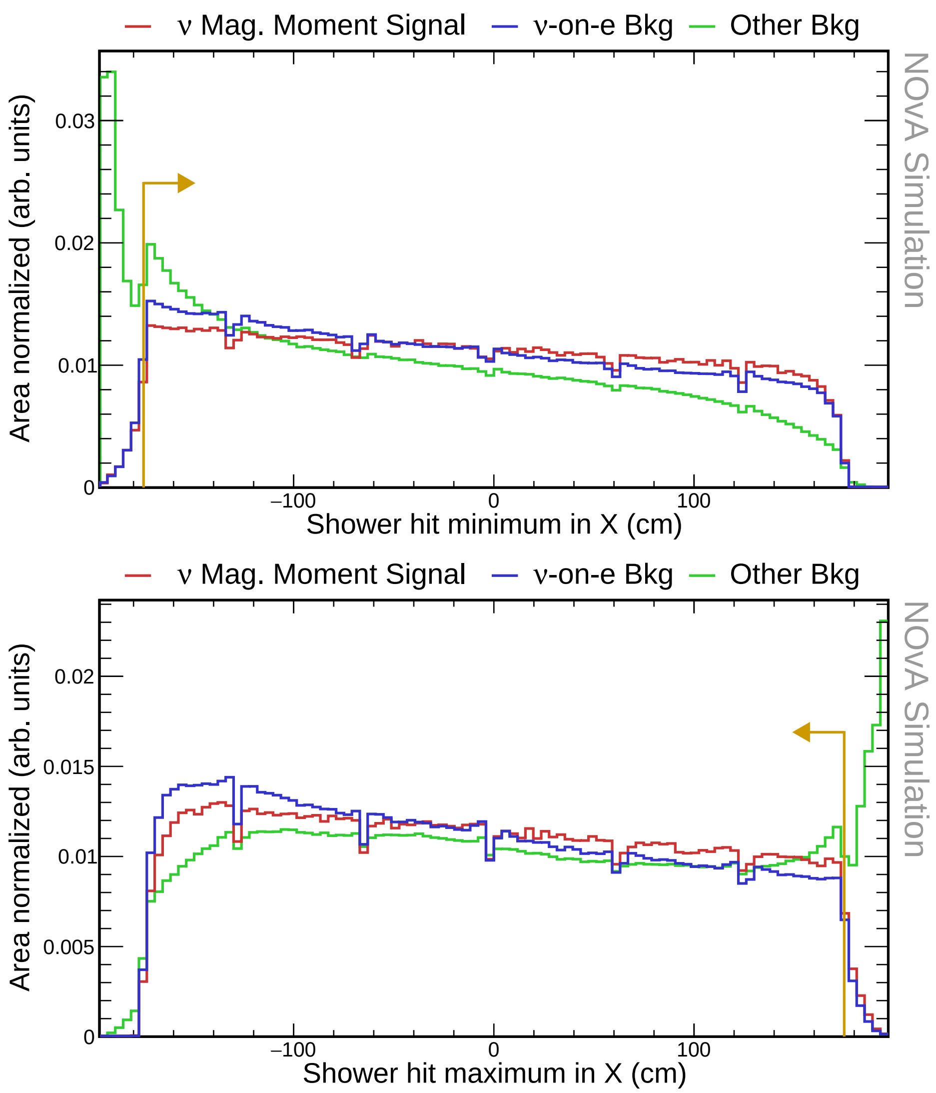

Figure 2.12: Relative comparison of signal, ν-on-e background, and other background events for the minimum and maximum position of the reconstructed shower along the x axis. Pre-selection and fiducial cuts were applied to make these plots. Gold lines show the values of the containment cuts.

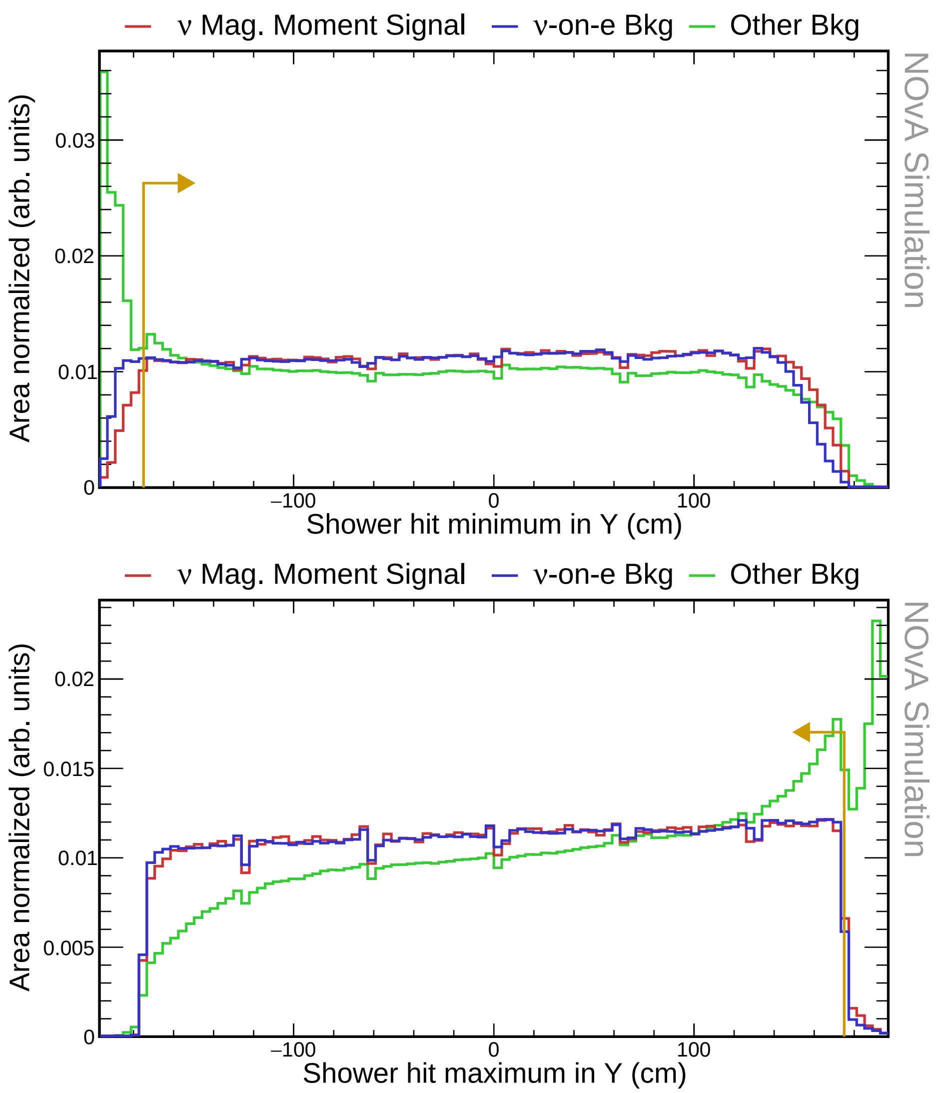

Figure 2.13: Relative comparison of signal, ν-on-e background, and other background events for the minimum and maximum position of the reconstructed shower along the Y axis. Pre-selection and fiducial cuts were applied to make these plots. Gold lines show the values of the containment cuts.

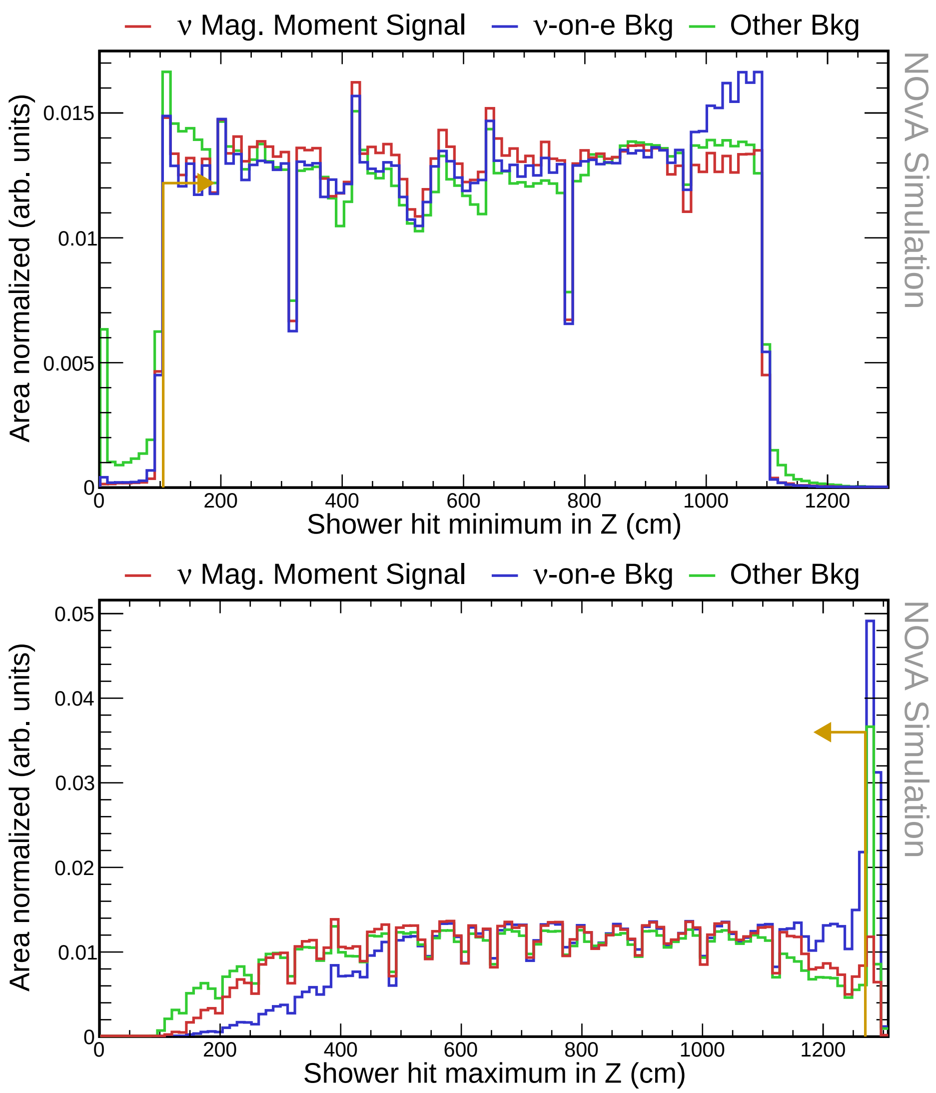

Figure 2.14: Relative comparison of signal, ν-on-e background, and other background events for the minimum and maximum position of the reconstructed shower along the Z axis. Pre-selection and fiducial cuts were applied to make these plots. Gold lines show the values of the containment cuts.

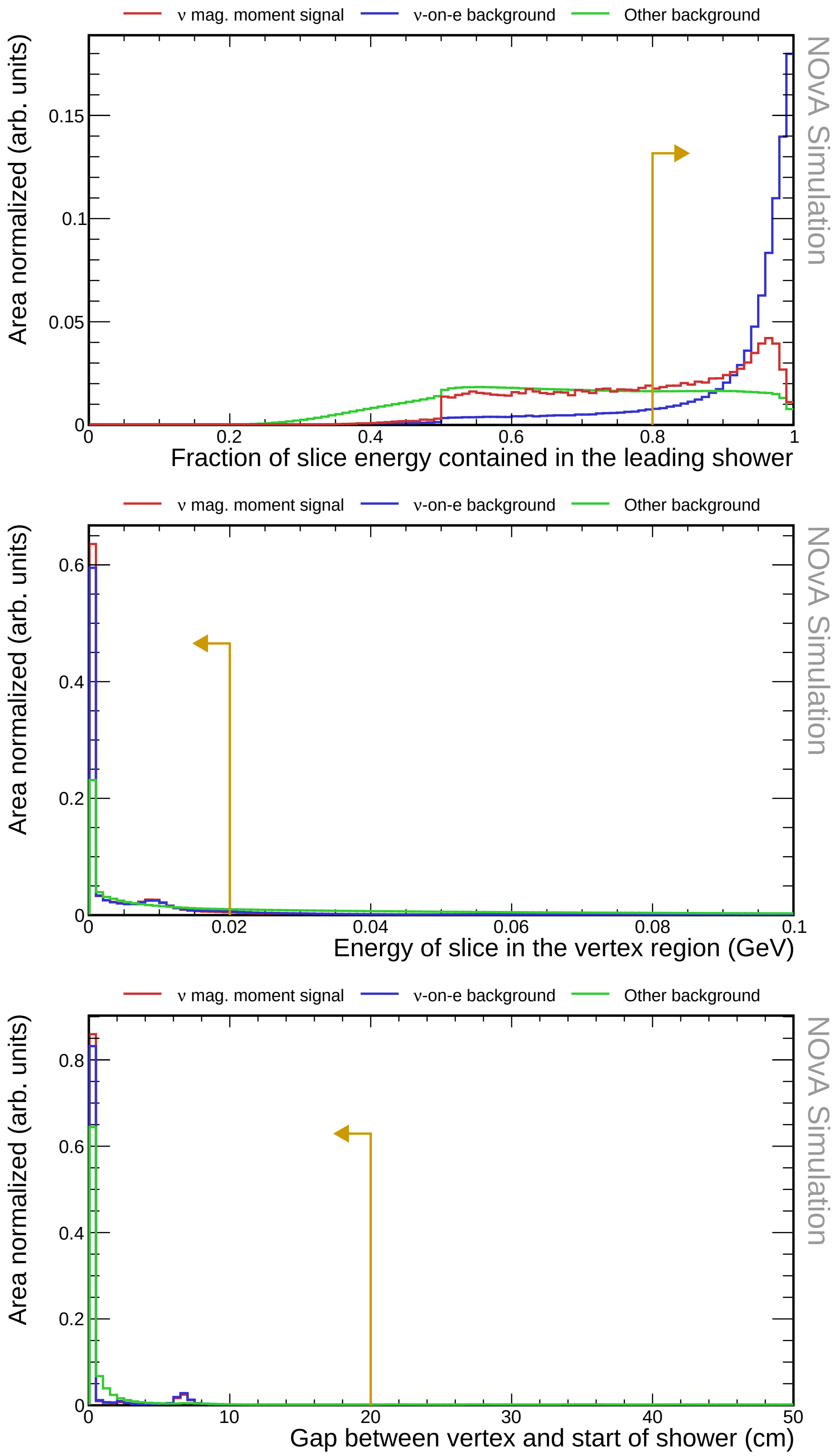

Figure 2.15: OLD Relative comparison of signal, ν-on-e background, and other background events for the reconstructed vertex. Every previous cut was applied to make these plots, including the ShwECont for the middle and the bottom plot and the VtxE cut for the bottom plot. Gold lines show the cut values that create the fiducial volume.

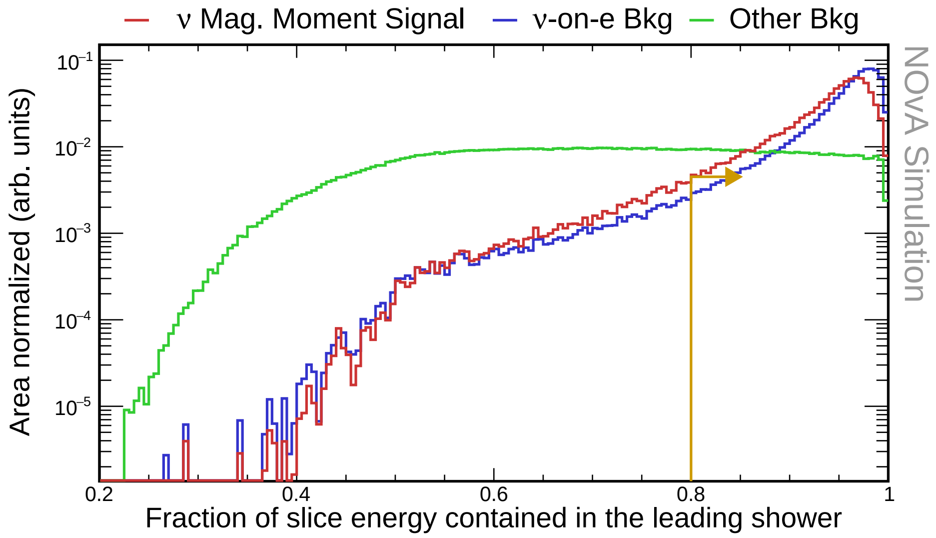

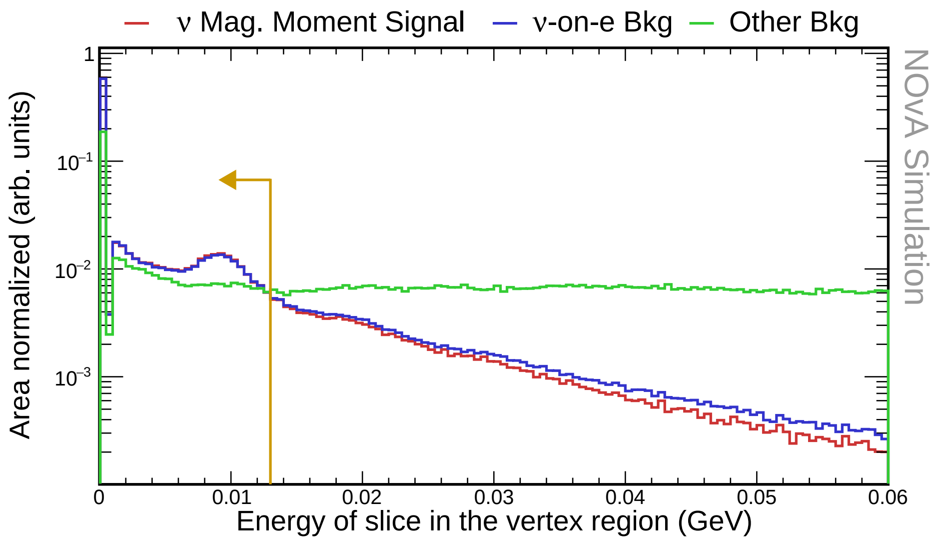

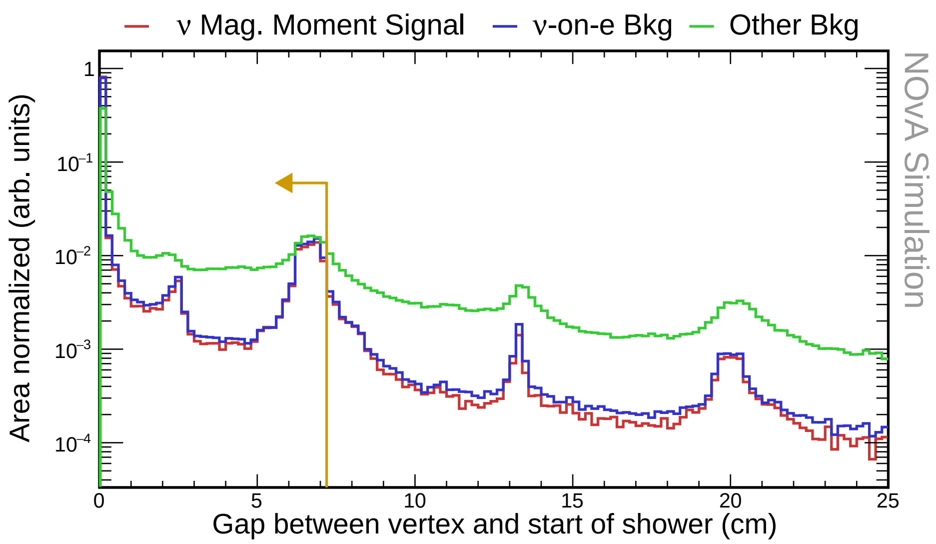

Figure 2.16: Relative comparison of signal, ν-on-e background, and other background events for the reconstructed vertex. No cuts were applied to make these plots. All the previous cuts were applied, including the cut on the shower energy. No single particle or event ID cuts were applied yet though. Gold lines show the cut values that create the fiducial volume.

Event classifiers

We are using two event classifiers based on convolution neural network that were developed specifically to identify ν-on-e interactions. The first one (`NuoneID`) is trained to select ν-on-e events and the second one (`Epi0ID`) is trained on the events passing the `NuoneID` to reject the π^0 background. Our selection requires that `NuoneID`>0.73 and that `Epi0ID`>0.92.

TO DO: *reference theory for the kinematics of nuone scattering* We require that the product of reconstructed energy of the primary shower and the square of its angle from the Z axis is $E_{cal}\theta^2 < 0.005$ GeV $\times$ rad^2.

TO DO: *Add plots of distributions of the event selection variables with two columns. LHS shows no cuts applied and RHS shows all previous cuts applied*

Using the many plots below that show the effect of each of the cuts on the signal and all background events. (For signal we are showing NuMM=...)

TO DO: *Describe the cutflow tables below* The final event count and efficiency of each of the cuts is shown on the table 2.4. Table 2.17 shows the dissemination of background into the individual components.

Table 2.4: Event selection cutflow table

Selection	ν Mag. Moment signal			ν-on-e background			Other background		
	N_{sig}	ϵ^{N-1}	ϵ (%)	N_{IBkg}	ϵ^{N-1}	ϵ (%)	N_{Bkg}	ϵ^{N-1}	ϵ (%)
No Cut	269.77	100	100	3.43×10^3	100	100	2.96×10^8	100	100
Vtx Is Valid	180.58	66.94	66.94	3.33×10^3	96.94	96.94	2.34×10^8	79.09	79.09
N Prongs	174.69	96.74	64.76	3.23×10^3	96.99	94.02	8.66×10^7	37.00	29.27
Png Length	174.67	99.99	64.75	3.22×10^3	99.64	93.68	7.67×10^7	88.56	25.92
N Planes	174.67	100	64.75	3.22×10^3	99.98	93.67	7.67×10^7	99.98	25.92
N Cells	174.67	100	64.75	3.22×10^3	99.98	93.65	7.42×10^7	96.78	25.08
Closest Slc	169.82	97.22	62.95	3.14×10^3	97.54	91.35	6.95×10^7	93.68	23.49
Fiducial	167.72	98.76	62.17	3.09×10^3	98.41	89.89	3.59×10^7	51.71	12.15
Cont.	159.37	95.02	59.08	2.48×10^3	80.43	72.30	1.38×10^7	38.35	4.66
ShwE Frac.	150.37	94.35	55.74	2.42×10^3	97.59	70.56	8.82×10^6	63.97	2.98
Vtx E	142.29	94.63	52.74	2.18×10^3	90.16	63.62	4.15×10^6	47.07	1.40
Shw Gap	137.96	96.96	51.14	2.09×10^3	95.58	60.80	3.25×10^6	78.34	1.10
Shw E	37.13	26.92	13.76	1.36×10^3	65.10	39.58	6.25×10^5	19.21	0.21
Nuoneid	29.48	79.39	10.93	940.21	69.18	27.38	2.42×10^4	3.88	8.19×10^{-3}
Epi0id	22.51	76.35	8.34	749.93	79.76	21.84	1.47×10^4	60.75	4.97×10^{-3}
$E\theta^2$	19.74	87.73	7.32	675.02	90.01	19.66	84.15	0.57	2.84×10^{-5}
$E\theta^2$ **(sb)**	2.74	-	1.01	74.30	-	2.16	1.01×10^3	-	3.43×10^{-4}
No ShwE	37.62	-	13.94	782.67	-	22.79	238.79	-	8.07E-05

TO DO: *Add a discussion of possible improvements on the event selection on its limitations - mostly for the analysis review committee* From here we can see that ... Maybe what can be improved is... This can likely be improved upon by specifically selection low energy events and removing the cut on the reconstructed shower energy.

2.4 Energy resolution and binning

TO DO: *Add the energy resolution and binning plots* Describe what events were used for the energy resolution study and how it was performed

What are the results

Final plot

The electron energy and angle distributions and resolutions. Are we going to fit in E, Th, or ETh2? Is there something else?

Show plots of Reco V True for both energy and angle. (Should I show it with or without the energy cut?). Also show the resolution plots.

2.5 Systematic uncertainties

2.6 Fitting and hypothesis testing, parameter estimation

What should be included here:

- Fit methodology: Detail the fitting techniques used to extract the muon neutrino magnetic moment from the data.
- Fit validation: Describe how the fit is validated, including any statistical tests used.
- Fake data studies: Explain the use of fake data or Monte Carlo simulations to test the robustness of the analysis.

Depends on what fits I'm going to end up using...

2.7 Results

Show the money plot - full prediction in the binned energy distribution, including the full statistical and systematic uncertainties

Write out the total number of measured events and their corresponding uncertainties

Explain what are the results of the fit and the limits, discuss the statistical significance of the result

2.8 Discussion

What should be included here:

- Interpretation: Interpret the results in the context of the current understanding of neutrino physics.
- Implications: Explain the broader implications of your findings for the field of particle physics.
- Future work: Suggest directions for future research based on your results.
  - Improvements in NOvA, more FHC data, including RHC data, better reconstruction, better simulation and calibration, better event selection, including sideband samples, more systematics studies, better fitting techniques...
  - Future beyond NOvA - DUNE
    - What are the possibilities for DUNE?

2.9 Conclusion

Summarize the results and compare them to the introduction, including comparisons to other experiments and theory. Restate the significant of the measurement

Closing remarks

Figure 2.17: Event selection cutflow table for background components

Selection	ν_eCC MEC			ν_eCC Other			ν_μCC			NC			Other		
	N	ϵ^{N-1}	ϵ (%)	N	ϵ^{N-1}	ϵ (%)	N	ϵ^{N-1}	ϵ (%)	N	ϵ^{N-1}	ϵ (%)	N	ϵ^{N-1}	ϵ (%)
No Cut	3.50×10^4	100	100	3.23×10^6	100	100	2.24×10^8	100	100	3.40×10^7	100.	100	3.49×10^7	100	100
Vtx Is Valid	3.27×10^4	93.58	93.58	2.62×10^6	81.14	81.14	1.99×10^8	89.02	89.02	2.57×10^7	75.55	75.55	6.53×10^6	18.70	18.70
N Prongs	2.74×10^4	83.76	78.39	1.39×10^6	53.05	43.05	6.75×10^7	33.89	30.17	1.51×10^7	58.57	44.25	2.65×10^6	40.51	7.58
Png Length	2.73×10^4	99.79	78.22	1.37×10^6	98.53	42.42	5.77×10^7	85.56	25.81	1.49×10^7	99.07	43.84	2.64×10^6	99.87	7.57
N Planes	2.73×10^4	99.99	78.22	1.37×10^6	99.99	42.41	5.77×10^7	99.98	25.81	1.49×10^7	100	43.84	2.64×10^6	100	7.57
N Cells	2.73×10^4	99.99	78.21	1.28×10^6	93.49	39.65	5.59×10^7	96.82	24.98	1.44×10^7	96.34	42.24	2.64×10^6	100	7.57
Closest Slc	2.73×10^4	99.79	78.05	1.21×10^6	94.25	37.37	5.33×10^7	95.40	23.84	1.35×10^7	94.17	39.77	1.43×10^6	54.22	4.10
Fiducial	1.39×10^4	51.12	39.90	6.30×10^5	52.10	19.47	2.60×10^7	48.77	11.62	8.25×10^6	60.99	24.26	1.05×10^6	73.53	3.02
Cont.	9.32×10^3	66.82	26.66	2.63×10^5	41.72	8.12	7.64×10^6	29.38	3.42	4.96×10^6	60.15	14.59	9.12×10^5	86.62	2.61
ShwE Frac.	9.20×10^3	98.70	26.32	1.95×10^5	74.39	6.04	4.82×10^6	63.10	2.15	2.97×10^6	59.78	8.72	8.28×10^5	90.81	2.37
Vtx E	5.92×10^3	64.33	16.93	6.05×10^4	30.96	1.87	1.97×10^6	40.79	0.88	1.36×10^6	45.75	3.99	7.62×10^5	92.03	2.18
Shw Gap	5.50×10^3	92.91	15.73	4.62×10^4	76.40	1.43	1.58×10^6	80.18	0.70	1.06×10^6	77.78	3.10	5.69×10^5	74.61	1.63
Shw E	3.62×10^3	65.81	10.35	1.12×10^4	24.15	0.35	4.38×10^5	27.80	0.20	1.71×10^5	16.15	0.50	1.28×10^3	0.23	3.68×10^{-3}
Nuoneid	1.40×10^3	38.63	4.00	2.11×10^3	18.89	0.065	1.17×10^4	2.66	5.21×10^{-3}	8.99×10^3	5.27	0.026	66.43	5.17	1.90×10^{-4}
Epi0id	1.14×10^3	81.78	3.27	1.61×10^3	76.40	0.050	7.17×10^3	61.52	3.20×10^{-3}	4.76×10^3	52.94	0.014	29.47	44.36	8.44×10^{-5}
$E\theta^2$	15.13	1.32	0.043	39.00	2.42	1.21×10^{-3}	8.62	0.12	3.85×10^{-6}	20.91	0.44	6.15×10^{-5}	0.50	1.69	1.43×10^{-6}
$E\theta^2$ **(sb)**	386.16	-	1.10	306.55	-	9.48×10^{-3}	165.59	-	7.40×10^{-5}	149.93	-	4.41×10^{-4}	6.24	-	1.79×10^{-5}
No ShwE	15.54	-	0.044	69.61	-	2.15×10^{-3}	68.48	-	3.06×10^{-5}	75.67	-	2.22×10^{-4}	9.49	-	2.72E-05

Acronyms

ν-on-e neutrino-on-electron. 24–27, 36, 37, 39–42, 44, 45

2p2h two particle - two hole. 10

ADC Analog-to-Digital Converter. 7, 14, 17, 18

APD Avalanche Photodiode. 5–7, 10, 17, 18, 46

ASIC Application-Specific Integrated Circuit. 7

BDT Boosted Decision Tree. 14

BPF Break Point Fitter. 12

BSM Beyond Standard Model. 24, 25, 27, 29, 32

CC Charged Current. 9–11, 36, 41, 42, 45, 49

CMC Comprehensive Model Configuration. 10

CNN Convolutional Neural Network. 13

COHπ Coherent π (production). 10

CP Charge conjugation - Parity (symmetry). 1

CRY Cosmic-Ray Shower Generator. 10, 14

CVN Convolutional Visual Network. 13

DAQ Data Acquisition. 7, 11, 16

DCM Data Concentration Module. 7, 8

DIS Deep Inelastic Scattering. 10

DUNE Deep Underground Neutrino Experiment. 1, 9, 24

FB Fibre Brightness. 17, 18

FD Far Detector. 3–7, 10, 11, 17–19, 22

FEB Front End Board. 6–8, 17, 46

Fermilab Fermi National Accelerator Laboratory. 1, 3, 9

FHC Forward Horn Current (neutrino mode). 2, 3

FOM Figure Of Merit. 46

FPGA Field Programmable Gate Array. 7

FSI Final State Interaction. 10

LDM Light Dark Matter. 26

LOWESS Locally Weighted Scatter plot Smoothing. 19, 20

MC Monte Carlo. 8–10, 14

MEC Meson Exchange Current. 10, 41, 45

MEU Muon Energy Unit. 21

MI Main Injector. 1, 2, 9

MIP Minimum Ionising Particle. 14, 18, 21

MIPP Main Injector Particle Production (experiment). 9

ML Machine Learning. 13, 14

NC Neutral Current. 11, 14, 42, 45

ND Near Detector. 1, 3–5, 7, 11, 12, 22, 24–26, 32, 41, 45

NDOS Near Detector on the Surface. 3

NOvA NuMI Off-axis ν_e Appearance (experiment). 1, 3–14, 16–22, 24–26, 32, 36, 38, 39, 41, 45

NP New Physics. 30

NuMI Neutrinos from the Main Injector. 1–3, 8, 9, 11, 25

PE Photo Electron. 6, 7, 15, 17–19

PECorr Corrected Photo Electrons. 19, 21

PID Particle Identification. 13

PMNS Pontecorvo-Maki-Nakagawa-Sakata. 29–31

POT Protons On Target. 2, 41

PPFX Package to Predict the Flux. 9, 23

PVC Polyvinyl chloride. 4–6, 22

QE Quasi Elastic (interaction). 9, 10

ReMId Reconstructed Muon Identifier. 14

Res Resonant baryon production. 9, 10

RHC Reverse Horn Current (antineutrino mode). 2, 3

SM Standard Model. 24, 27–30, 36–41

WLS Wavelength Shifting (fibre). 5, 6, 10, 14, 16, 18, 21

Bibliography

[1] Nova experiments official website. URL https://novaexperiment.fnal.gov. Cited February 2024.

[2] Fermi national accelerator laboratory official website. URL https://fnal.gov. Cited February 2024.

[3] Gary Feldman for the NOvA Collaboration. Physics of the nova experiment. White paper, 2012. URL https://nova-docdb.fnal.gov/cgi-bin/ShowDocument?docid=7733. Public NOvA document: NOVA-doc-7733-v1, cited on 05.2020.

[4] R.B. Patterson. The NOvA Experiment: Status and Outlook. *Nucl. Phys. B Proc. Suppl.*, 235-236:151–157, 2013. doi:10.1016/j.nuclphysbps.2013.04.005.

[5] P. Adamson et al. First measurement of muon-neutrino disappearance in NOvA. *Phys. Rev. D*, 93(5):051104, 2016. doi:10.1103/PhysRevD.93.051104.

[6] M.A. Acero et al. First Measurement of Neutrino Oscillation Parameters using Neutrinos and Antineutrinos by NOvA. *Phys. Rev. Lett.*, 123(15):151803, 2019. doi:10.1103/PhysRevLett.123.151803.

[7] M. A. Acero et al. Improved measurement of neutrino oscillation parameters by the NOvA experiment. *Phys. Rev. D*, 106(3):032004, 2022. doi:10.1103/PhysRevD.106.032004.

[8] M. A. Acero et al. Measurement of neutrino-induced neutral-current coherent π^0 production in the NOvA near detector. *Phys. Rev. D*, 102(1):012004, 2020. doi:10.1103/PhysRevD.102.012004.

[9] M. A. Acero et al. Measurement of the double-differential muon-neutrino charged-current inclusive cross section in the NOvA near detector. *Phys. Rev. D*, 107(5):052011, 2023. doi:10.1103/PhysRevD.107.052011.

[10] M. A. Acero et al. Measurement of the ν_e-Nucleus Charged-Current Double-Differential Cross Section at $\langle E_\nu \rangle = 2.4$ GeV using NOvA. *Phys. Rev. Lett.*, 130 (5):051802, 2023. doi:10.1103/PhysRevLett.130.051802.

[11] M. A. Acero et al. Measurement of ν_μ charged-current inclusive π^0 production in the NOvA near detector. *Phys. Rev. D*, 107(11):112008, 2023. doi:10.1103/PhysRevD.107.112008.

[12] P. Adamson et al. Search for active-sterile neutrino mixing using neutral-current interactions in NOvA. *Phys. Rev. D*, 96(7):072006, 2017. doi:10.1103/PhysRevD.96.072006.

[13] M. A. Acero et al. Search for Active-Sterile Antineutrino Mixing Using Neutral-Current Interactions with the NOvA Experiment. *Phys. Rev. Lett.*, 127(20):201801, 2021. doi:10.1103/PhysRevLett.127.201801.

[14] M. A. Acero et al. Supernova neutrino detection in NOvA. *JCAP*, 10:014, 2020. doi:10.1088/1475-7516/2020/10/014.

[15] M. A. Acero et al. Extended search for supernovalike neutrinos in NOvA coincident with LIGO/Virgo detections. *Phys. Rev. D*, 104(6):063024, 2021. doi:10.1103/PhysRevD.104.063024.

[16] M. A. Acero et al. Search for slow magnetic monopoles with the NOvA detector on the surface. *Phys. Rev. D*, 103(1):012007, 2021. doi:10.1103/PhysRevD.103.012007.

[17] Peter N. Shanahan and Patricia LaVern Vahle. Physics with NOvA: a half-time review. *Eur. Phys. J. ST*, 230(24):4259–4273, 2021. doi:10.1140/epjs/s11734-021-00285-9.

[18] Peter Shanahan and Patricia Vahle. The NOvA Physics Program through 2025. Snowmass 2021 Letters of Interest NF, 135. URL https://www.snowmass21.org/docs/files/summaries/NF/SNOWMASS21-NF1_NF3_Patricia_Vahle-145.pdf.

[19] P. Adamson et al. The NuMI Neutrino Beam. *Nucl. Instrum. Meth. A*, 806:279–306, 2016. doi:10.1016/j.nima.2015.08.063.

[20] Records. URL https://operations.fnal.gov/records/. Performance records achieved by the Fermilab accelerators. Cited May 2024.

[21] Katsuya Yonehara. Megawatt upgrade of numi target system. 1 2022. URL https://www.osti.gov/biblio/1844332.

[22] Leonidas Aliaga Soplin. *Neutrino Flux Prediction for the NuMI Beamline.* PhD thesis, William-Mary Coll., 2016.

[23] Leonidas Aliaga Soplin. 2017-2018 Beam Plots. NOVA Document 20843. URL https://nova-docdb.fnal.gov/cgi-bin/sso/ShowDocument?docid=20843. NOvA internal document.

[24] D. S. Ayres et al. The nova technical design report. *NOvA Collaboration*, 2007. doi:10.2172/935497.

[25] Yury Kudenko. Neutrino detectors for oscillation experiments. *JINST*, 12(06): C06003, 2017. doi:10.1088/1748-0221/12/06/C06003.

[26] S. Mufson et al. Liquid scintillator production for the NOvA experiment. *Nucl. Instrum. Meth. A*, 799:1–9, 2015. doi:10.1016/j.nima.2015.07.026.

[27] Alex Sousa. Density of NOvA Liquid Scintillator at 69° F. NOVA Document 11886. URL https://nova-docdb.fnal.gov/cgi-bin/sso/ShowDocument?docid=11886. NOvA internal document.

[28] M.J. Berger, J.S. Coursey, M.A. Zucker, and J. Chang. ESTAR, PSTAR, and ASTAR: Computer Programs for Calculating Stopping-Power and Range Tables for Electrons, Protons, and Helium Ions (version 1.2.3). URL http://physics.nist.gov/Star.

[29] Luke Vinton. Calorimetric Energy Scale Calibration of the NOvA Detectors. NOVA Document 13579, document FA_Calorimetric_energy_scale.pdf. URL https://nova-docdb.fnal.gov/cgi-bin/sso/ShowDocument?docid=13579. NOvA Technical Note.

[30] Xinchun Tian. NOvA Data Acquisition Software System. In *Meeting of the APS Division of Particles and Fields*, 9 2011.

[31] Joao Coelho, Barnali Chowdhury, and Ryan Murphy. Tech note: Good data selection. NOVA Document 13546. URL https://nova-docdb.fnal.gov/cgi-bin/sso/ShowDocument?docid=13546. NOvA technical note.

[32] Jonathan M. Paley. BadChannels Technical Note. NOVA Document 12771. URL https://nova-docdb.fnal.gov/cgi-bin/sso/ShowDocument?docid=12771. NOvA technical note.

[33] A. Aurisano, C. Backhouse, R. Hatcher, N. Mayer, J. Musser, R. Patterson, R. Schroeter, and A. Sousa. The NOvA simulation chain. *J. Phys. Conf. Ser.*, 664(7):072002, 2015. doi:10.1088/1742-6596/664/7/072002.

[34] S. Agostinelli et al. GEANT4–a simulation toolkit. *Nucl. Instrum. Meth. A*, 506: 250–303, 2003. doi:10.1016/S0168-9002(03)01368-8.

[35] Zarko Pavlovic. *Observation of Disappearance of Muon Neutrinos in the NuMI Beam.* PhD thesis, Texas U., 2008.

[36] L. Aliaga et al. Neutrino Flux Predictions for the NuMI Beam. *Phys. Rev. D*, 94 (9):092005, 2016. doi:10.1103/PhysRevD.94.092005. [Addendum: Phys.Rev.D 95, 039903 (2017)].

[37] C. Alt et al. Inclusive production of charged pions in p+C collisions at 158-GeV/c beam momentum. *Eur. Phys. J. C*, 49:897–917, 2007. doi:10.1140/epjc/s10052-006-0165-7.

[38] Gemma Maria Tinti. *Sterile neutrino oscillations in MINOS and hadron production in pC collisions.* PhD thesis, 2010.

[39] B Baatar, G Barr, J Bartke, L Betev, O Chvala, J Dolejsi, V Eckardt, HG Fischer, Z Fodor, A Karev, et al. Inclusive production of protons, anti-protons, neutrons, deuterons and tritons in p+ c collisions at 158 gev/c beam momentum. *The European Physical Journal C*, 73:1–66, 2013. doi:10.1140/epjc/s10052-013-2364-3.

[40] D. S. Barton et al. Experimental study of the a dependence of inclusive hadron fragmentation. *Phys. Rev. D*, 27:2580–2599, Jun 1983. doi:10.1103/PhysRevD.27.2580.

[41] Andrey V. Lebedev. *Ratio of Pion Kaon Production in Proton Carbon Interactions.* PhD thesis, 2007.

[42] T.T. Böhlen, F. Cerutti, M.P.W. Chin, A. Fassò, A. Ferrari, P.G. Ortega, A. Mairani, P.R. Sala, G. Smirnov, and V. Vlachoudis. The fluka code: Developments and challenges for high energy and medical applications. *Nuclear Data Sheets*, 120: 211–214. ISSN 0090-3752. doi:10.1016/j.nds.2014.07.049.

[43] Alfredo Ferrari, Paola R. Sala, Alberto Fasso, and Johannes Ranft. FLUKA: A multi-particle transport code (Program version 2005). 10 2005. doi:10.2172/877507.

[44] A. Aduszkiewicz et al. Measurements of production and inelastic cross sections for p+C , p+Be , and p+Al at 60 GeV/c and p+C and p+Be at 120 GeV/c. *Phys. Rev. D*, 100(11):112001, 2019. doi:10.1103/PhysRevD.100.112001.

[45] H. Adhikary et al. Measurements of π^+, π^-, p, $\bar{p}$, K^+ and K^- production in 120 GeV/c p + C interactions. *Phys. Rev. D*, 108:072013, 2023. doi:10.1103/PhysRevD.108.072013.

[46] H. Adhikary et al. Measurements of KS0, Λ, and Λ^- production in 120 GeV/c p+C interactions. *Phys. Rev. D*, 107(7):072004, 2023. doi:10.1103/PhysRevD.107.072004.

[47] A. Aduszkiewicz et al. Measurements of hadron production in π^+ + C and π^+ + Be interactions at 60 GeV/c. *Phys. Rev. D*, 100(11):112004, 2019. doi:10.1103/PhysRevD.100.112004.

[48] Matej Pavin. Hadron production measurements for neutrino experiments, 2020. URL https://indico.fnal.gov/event/43209/contributions/187869/attachments/130502/159028/HadronProduction_neutrino2020.pdf. Presented on Neutrino 2020 conference.

[49] T. Akaishi et al. EMPHATIC: A Proposed Experiment to Measure Hadron Scattering and Production Cross Sections for Improved Neutrino Flux Predictions. 12 2019.

[50] C. Andreopoulos et al. The GENIE Neutrino Monte Carlo Generator. *Nucl. Instrum. Meth. A*, 614:87–104, 2010. doi:10.1016/j.nima.2009.12.009.

[51] J. Nieves, J. E. Amaro, and M. Valverde. Inclusive quasielastic charged-current neutrino-nucleus reactions. *Phys. Rev. C*, 70:055503, Nov 2004. doi:10.1103/PhysRevC.70.055503.

[52] Aaron S. Meyer, Minerba Betancourt, Richard Gran, and Richard J. Hill. Deuterium target data for precision neutrino-nucleus cross sections. *Phys. Rev. D*, 93:113015, Jun 2016. doi:10.1103/PhysRevD.93.113015.

[53] J. Nieves, I. Ruiz Simo, and M. J. Vicente Vacas. Inclusive charged-current neutrino-nucleus reactions. *Phys. Rev. C*, 83:045501, Apr 2011. doi:10.1103/PhysRevC.83.045501.

[54] R. Gran, J. Nieves, F. Sanchez, and M. J. Vicente Vacas. Neutrino-nucleus quasi-elastic and 2p2h interactions up to 10 gev. *Phys. Rev. D*, 88:113007, Dec 2013. doi:10.1103/PhysRevD.88.113007.

[55] Ch. Berger and L. M. Sehgal. Lepton mass effects in single pion production by neutrinos. *Phys. Rev. D*, 76:113004, Dec 2007. doi:10.1103/PhysRevD.76.113004.

[56] Ch. Berger and L. M. Sehgal. Partially conserved axial vector current and coherent pion production by low energy neutrinos. *Phys. Rev. D*, 79:053003, Mar 2009. doi:10.1103/PhysRevD.79.053003.

[57] A Bodek and U. K. Yang. Higher twist, xi(omega) scaling, and effective LO PDFs for lepton scattering in the few GeV region. *J. Phys. G*, 29:1899–1906, 2003. doi:10.1088/0954-3899/29/8/369.

[58] T. Yang, C. Andreopoulos, H. Gallagher, K. Hoffmann, and P. Kehayias. A Hadronization Model for Few-GeV Neutrino Interactions. *Eur. Phys. J. C*, 63:1–10, 2009. doi:10.1140/epjc/s10052-009-1094-z.

[59] L.L. Salcedo, E. Oset, M.J. Vicente-Vacas, and C. Garcia-Recio. Computer simulation of inclusive pion nuclear reactions. *Nuclear Physics A*, 484(3):557–592. ISSN 0375-9474. doi:10.1016/0375-9474(88)90310-7.

[60] Chris Hagmann, David Lange, and Douglas Wright. Cosmic-ray shower generator (cry) for monte carlo transport codes. volume 2, pages 1143 – 1146. ISBN 978-1-4244-0922-8. doi:10.1109/NSSMIC.2007.4437209.

[61] C. N. Chou. The nature of the saturation effect of fluorescent scintillators. *Phys. Rev.*, 87:904–905, Sep 1952. doi:10.1103/PhysRev.87.904.

[62] M. Baird, J. Bian, M. Messier, E. Niner, D. Rocco, and K. Sachdev. Event Reconstruction Techniques in NOvA. *J. Phys. Conf. Ser.*, 664(7):072035, 2015. doi:10.1088/1742-6596/664/7/072035.

[63] Martin Ester, Hans-Peter Kriegel, Jörg Sander, and Xiaowei Xu. A density-based algorithm for discovering clusters in large spatial databases with noise. In *Proceedings of the Second International Conference on Knowledge Discovery and Data Mining*, KDD'96, page 226–231. AAAI Press, 1996. doi:10.5555/3001460.3001507.

[64] Leandro A. F. Fernandes and Manuel Menezes de Oliveira Neto. Real-time line detection through an improved hough transform voting scheme. *Pattern Recognit.*, 41:299–314, 2008. doi:10.1016/j.patcog.2007.04.003. URL https://api.semanticscholar.org/CorpusID:5996185.

[65] Mattias Ohlsson, Carsten Peterson, and Alan L. Yuille. Track finding with deformable templates — the elastic arms approach. *Computer Physics Communications*, 71(1):77–98. ISSN 0010-4655. doi:10.1016/0010-4655(92)90074-9. URL https://www.sciencedirect.com/science/article/pii/0010465592900749.

[66] R. Krishnapuram and J.M. Keller. A possibilistic approach to clustering. *IEEE Transactions on Fuzzy Systems*, 1(2):98–110, 1993. doi:10.1109/91.227387.

[67] Miin-Shen Yang and Kuo-Lung Wu. Unsupervised possibilistic clustering. *Pattern Recognition*, 39(1):5–21. ISSN 0031-3203. doi:https://doi.org/10.1016/j.patcog.2005.07.005. URL https://www.sciencedirect.com/science/article/pii/S0031320305002943.

[68] Jianming Bian, Hongyue Duyang, and Alexander Radovic. Blessing package for Neutrino-Electron Scattering and Coherent Pi0. NOVA Document 13862. URL https://nova-docdb.fnal.gov/cgi-bin/sso/ShowDocument?docid=13862. NOvA internal document.

[69] Nicholas Jacob Raddatz. *Measurement of Muon Neutrino Disappearance with Non-Fiducial Interactions in the NOνA Experiment.* PhD thesis, Minnesota U., 2016.

[70] Michael David Baird. *An Analysis of Muon Neutrino Disappearance from the NuMI Beam Using an Optimal Track Fitter.* PhD thesis, Indiana U., 2015.

[71] G. Lutz. Optimum track fitting in the presence of multiple scattering. *Nuclear Instruments and Methods in Physics Research Section A: Accelerators, Spectrometers, Detectors and Associated Equipment*, 273(1):349–361. ISSN 0168-9002. doi:https://doi.org/10.1016/0168-9002(88)90836-4. URL https://www.sciencedirect.com/science/article/pii/0168900288908364.

[72] Brian Rebel. Window tracking algorithm for cosmic ray muons. NOVA Document 15977-v1. URL https://nova-docdb.fnal.gov/cgi-bin/sso/ShowDocument?docid=15977. NOvA internal document.

[73] Christian Szegedy, Wei Liu, Yangqing Jia, Pierre Sermanet, Scott Reed, Dragomir Anguelov, Dumitru Erhan, Vincent Vanhoucke, and Andrew Rabinovich. Going Deeper with Convolutions. *arXiv e-prints*, art. arXiv:1409.4842. doi:10.48550/arXiv.1409.4842.

[74] A. Aurisano, A. Radovic, D. Rocco, A. Himmel, M.D. Messier, E. Niner, G. Pawloski, F. Psihas, A. Sousa, and P. Vahle. A Convolutional Neural Network Neutrino Event Classifier. *JINST*, 11(09):P09001, 2016. doi:10.1088/1748-0221/11/09/P09001.

[75] Fernanda Psihas. Measurement of long baseline neutrino oscillations and improvements from deep learning. 1 2018. doi:10.2172/1437288. URL https://www.osti.gov/biblio/1437288.

[76] Prabhjot Singh. *Extraction of Neutrino Oscillation Parameters using a Simultaneous Fit of ν_μ Disappearance and ν_e Appearance data with the NOvA Experiment.* PhD thesis, University of Delhi, Dept. of Physics and Astrophysics, India, Delhi U., 9 2019.

[77] Ryan J. Nichol. Fibre brightness from cosmic muon data. NOVA Document 34909. URL https://nova-docdb.fnal.gov/cgi-bin/sso/ShowDocument?docid=34909. NOvA technical note.

[78] Prabhjot Singh. Attenuation Calibration of the NOvA Detectors. In *The 38th International Conference on High Energy Physics (ICHEP 2016)*, 2024. URL https://nova-docdb.fnal.gov/cgi-bin/sso/ShowDocument?docid=15840. (cited on 03.2024).

[79] R. L. Workman and Others. Review of Particle Physics. *PTEP*, 2022:083C01, 2022. doi:10.1093/ptep/ptac097.

[80] L. B. Auerbach et al. Measurement of electron-neutrino electron elastic scattering. *Phys. Rev. D*, 63:112001. doi:10.1103/PhysRevD.63.112001.

[81] E. Aprile et al. Excess electronic recoil events in XENON1T. *Phys. Rev. D*, 102:072004, . doi:10.1103/PhysRevD.102.072004.

[82] E. Aprile et al. Search for New Physics in Electronic Recoil Data from XENONnT. *Phys. Rev. Lett.*, 129:161805, . doi:10.1103/PhysRevLett.129.161805.

[83] M. Atzori Corona, W. M. Bonivento, M. Cadeddu, N. Cargioli, and F. Dordei. New constraint on neutrino magnetic moment and neutrino millicharge from LUX-ZEPLIN dark matter search results. *Phys. Rev. D*, 107:053001. doi:10.1103/PhysRevD.107.053001.

[84] M. Agostini et al. Limiting neutrino magnetic moments with borexino phase-ii solar neutrino data. *Phys. Rev. D*, 96:091103. doi:10.1103/PhysRevD.96.091103.

[85] Amir N. Khan. Light new physics and neutrino electromagnetic interactions in XENONnT. *Physics Letters B*, 837:137650. ISSN 0370-2693. doi:10.1016/j.physletb.2022.137650. URL https://www.sciencedirect.com/science/article/pii/S0370269322007845.

[86] K. S. Babu, Sudip Jana, and Manfred Lindner. Large Neutrino Magnetic Moments in the Light of Recent Experiments. *JHEP*, 10:040. doi:10.1007/JHEP10(2020)040.

[87] Biao Wang. *Muon-Neutrino Electron Elastic Scattering and a Search for the Muon-Neutrino Magnetic Moment in the NOvA Near Detector*. PhD thesis. URL https://scholar.smu.edu/hum_sci_physics_etds/1.

[88] Wenjie Wu and Yiwen Xiao. Constraint of the Integrated Neutrino Flux from Neutrino-Electron Elastic Scattering in the NOvA Near Detector. NOVA Document 56383. URL https://nova-docdb.fnal.gov/cgi-bin/sso/ShowDocument?docid=56383. NOvA technical note.

[89] Barnali Brahma, Tyler Horoho, and Mu Wei. TechNote: Light Dark Matter Search with NOvA Near Detector. NOVA Document 59439. URL https://nova-docdb.fnal.gov/cgi-bin/sso/ShowDocument?docid=59439. NOvA technical note.

[90] Athula Wickremasinghe, Wenjie Wu, and Yiwen Xiao. Status of the Measurement of Neutrino-Electron Elastic Scattering in the NOvA Near Detector. In *Neutrino 2022*. URL https://indico.kps.or.kr/event/30/contributions/738/.

[91] Patrick Huber et al. Snowmass Neutrino Frontier Report. In *Snowmass 2021*, 11 2022.

[92] Carlo Giunti and Alexander Studenikin. Neutrino electromagnetic interactions: A window to new physics. *Rev. Mod. Phys.*, 87:531–591, Jun 2015. doi:10.1103/RevModPhys.87.531.

[93] Boris Kayser. Majorana neutrinos and their electromagnetic properties. *Phys. Rev. D*, 26:1662–1670, Oct 1982. doi:10.1103/PhysRevD.26.1662.

[94] José F. Nieves. Electromagnetic properties of majorana neutrinos. *Phys. Rev. D*, 26:3152–3158, Dec 1982. doi:10.1103/PhysRevD.26.3152.

[95] Carlo Giunti, Julieta Gruszko, Benjamin Jones, Lisa Kaufman, Diana Parno, and Andrea Pocar. Report of the Topical Group on Neutrino Properties for Snowmass 2021. 9 2022.

[96] Nicole F. Bell, Mikhail Gorchtein, Michael J. Ramsey-Musolf, Petr Vogel, and Peng Wang. Model independent bounds on magnetic moments of Majorana neutrinos. *Phys. Lett. B*, 642:377–383, 2006. doi:10.1016/j.physletb.2006.09.055.

[97] Leonidas Aliaga, Derek Doyle, Matthew Judah, Norm Buchanan, Linda Cremonesi, Mat Muether, and Jon Paley. Measurement of the Double-Differential

Inclusive Electron-Neutrino Charged-Current Cross Section in the NOvA Near Detector. NOVA Document 37668, 04 2020. URL https://nova-docdb.fnal.gov/cgi-bin/sso/ShowDocument?docid=37668. NOvA technical note.